# Stony Brook University

# Toward Metal-Free Magnetic Micro-Graphite as Contrast Agents for Magnetic Resonance Imaging: Synthesis, Characterization and In vitro Studies

by

**Saathyaki Rajamani**

to

The Graduate School

in Partial Fulfillment of the

Requirements

for the degree of

**Master of Science**

in

**Biomedical Engineering**

Stony Brook University

May 2010

Stony Brook University

The Graduate School

Saathyaki Rajamani

We the thesis committee for the above candidate for the Master of Science degree, hereby recommend acceptance of this thesis.

**Dr. Balaji Sitharaman**, Assistant Professor

Thesis Advisor, Department of Biomedical Engineering

**Dr. Michael Hadjiargyrou**, Associate Professor

Chair of Defense, Department of Biomedical Engineering, Genetics, and Orthopedics

**Dr. Helmut Strey**, Associate Professor

Graduate Program Director, Department of Biomedical Engineering

This thesis is accepted by the Graduate School

Lawrence Martin

Dean of the Graduate School

Abstract of the thesis

**Toward Metal-Free Magnetic Micro-Graphite as Contrast Agents for Magnetic Resonance Imaging: Synthesis, Characterization and In vitro Studies**

by

**Saathyaki Rajamani**

Master of Science

in

Biomedical Engineering

Stony Brook University

2010

Approximately sixty million MRI procedures are performed annually worldwide, with 30% of these procedures using MRI contrast agents (CAs). Most commonly used clinical CAs and experimental CAs for advance molecular/cellular MRI are either paramagnetic Gd-based T1 CAs or superparamagnetic Fe-based T2 CAs. They use chelating ligands or biocompatible coatings to sequester the toxicity of naked gadolinium (Gd) and iron (Fe). But, these toxicity-sequestering strategies may not be adequate as recent reports associate clinical Gd-based agents CAs with acute renal failure. Graphitic carbon in general, is safer than naked Gd or Fe, and thus, the possibility of creating metal-free magnetic carbon CAs in a systematic and controllable way will be an exciting and tantalizing

prospect. Magnetism in graphitic structures has been recently reported at room temperatures. Experimental methods adopted to induce magnetism in graphite, including the introduction of defects by irradiation of ions or electrons yield microscopic quantities of magnetic graphite. Due to poor scalability and low yields of the synthesis techniques, accurate characterization of magnetic graphite samples is challenging. Further, the presence of metallic impurities questions the very origin of magnetism in graphite, a concern yet to be comprehensively addressed.

Here, a novel synthesis technique for the production of macroscopic quantities of magnetic graphite with ease of scalability is presented. This chemical synthesis technique involves fluorination of graphite samples, subjected to pyrolysis to introduce defects and followed by hydrogenation of these defect sites. Analytical grade micro-graphite particles were used for these studies. The micro-graphite samples were superparamagnetic at room temperature with magnetization values around 3-6 orders higher than other published data. Saturation magnetization for micro-graphite of about 1.5emu/g, comparable to theoretical predicted value is observed. Absence of magnetism in micro-graphite samples at all processing steps prior to hydrogenation indicates that any trace metallic impurities do not induce magnetism. Structural characterization of magnetic micro-graphite samples using spectroscopic techniques revealed an increase in the number of defects and introduction of hydrogen bonds.

Relaxometry and phantom imaging studies performed on magnetic micro-graphite samples to evaluate their contrast enhancing abilities showed better reduction in spin-spin (T2) relaxation times compared to spin-lattice (T1) relaxation times. Concurrently, MRI phantom imaging studies performed to visually evaluate their efficiency as contrast

agents indicated enhancement in contrast comparable to clinically used Magnevist by shortening of T2 relaxation times. Preliminary in vitro cytotoxicity studies indicate that micro-graphite showed significantly higher cell viability at the highest treatment concentration (80ng/ml) at the end of 24 hours compared to metals commonly used in contrast agents.

The higher magnetization values, better yields and, the promising in vitro MRI and cytotoxicity studies on the magnetic micro-graphite open venues for their possible application as CAs for MRI.

## Table of Contents

**List of Figures**

## List of Tables

## Preface

## Hypothesis and Specific Aims

***1. Hydrogenation of defect sites induces magnetism in graphitic structures***

**Specific Aim 1.1:** Develop a chemical synthesis technique for defect creation and hydrogenation in micro-graphite particles to induce magnetism.

**Specific Aim 1.2:** Confirm the magnetic behavior of micro-graphite particles and determine corresponding magnetization values.

***2. Magnetic graphite particles shorten T1 and T2 relaxation times, and enhance contrast in Magnetic Resonance Imaging***

**Specific Aim 2.1:** Perform relaxometry studies to evaluate the influence of magnetic micro-graphite particles on spin-lattice and spin-spin relaxation times.

**Specific Aim 2.2:** Qualitatively evaluate using MRI the contrast enhancing performance of magnetic micro-graphite particles.

***3. Graphite particles are less cytotoxic compared to metals ions commonly used in contrast agents for Magnetic Resonance Imaging***

**Specific Aim 3:** Evaluate the function of concentration on viability of macrophage cells treated with graphite and metals ions commonly used in MRI contrast agents

**Acknowledgements**

I would like to thank my mentor and advisor Dr. Balaji Sitharaman, for his encouragement, dedication and critical insights throughout my research. I am ever grateful to him for giving me the opportunity to work on this wonderful project.

I would like to take this opportunity to thank Dr. Michael Hadjiargyrou for his continued support and advice during the course of my study at Stony Brook University. I am grateful to Dr. Helmut Strey for serving on my thesis committee.

I would like to acknowledge the immense help and support rendered by Dr. Mikhail Feygenson, Brookhaven National Laboratories, for the SQUID measurements and discussions. I thank Dr. Meigan Aronson, Brookhaven National Laboratories for providing time for SQUID measurements and her valuable comments towards this project. I also would like to acknowledge the help from Dr. Cherno Jaye, Brookhaven Laboratories for his help with the NEXAFS data.

Special thanks to Christopher Jenson and Tom Salagaj, First Nano/CVD Research labs for their patience and efforts in synthesizing magnetic graphite particles.

I would like to thank Dr. Pramod Avti, our lab post doc and a very good friend who has been supportive and helpful from the start of my research. I thank him for his patience, tutoring and valuable comments for this thesis work, especially with the in vitro studies.

I am very thankful to Maggie Swierczewska, for teaching me various sample preparation techniques for SQUID, Raman microscopy and NMRD studies, and acknowledge her help and support with data measurements and discussions for the above.

I thank my dear friends Sujatha Sivakumar, Vishal Ravikumar, Smaran Madheshwara, Ashish Taskar, Arvind Ayyangar and Aditi Jatkar who have continued to support and motivate me during the course of my thesis.

Finally, I thank my lovely parents Jayshree and Rajamani and my dear little sister Saathvika, for their love and to whom I dedicate this work.

# Chapter 1: Magnetic Graphite

## 1.1. Background and Significance

The phenomenon of magnetism lies in the foundations of many technological advancements and innovations. Ranging from medical imaging to data storage, magnetic materials constantly find newer applications across various fields. Magnetism was first observed in iron and later on in nickel and cobalt. Historically associated only with metals, magnetism has been recently reported in materials of non-metallic composition.(*1*) The demonstration of metal free magnetism in graphitic carbon has generated great interest among researchers across various fields including biology, physics, nanotechnology and electronics.(*2*)

Carbon, a tetravalent element with four available electrons for bonding, confers unique properties to form various allotropes. Besides diamond and graphite other carbon allotropes have been recently discovered that include fullerenes, carbon nanotubes and carbon nanofoams.(*3-5*) The allotropes vary significantly in their physical properties, making them ideal for a variety of applications.(*6*) Graphite is the most stable and abundant allotrope of carbon. It consists of hexagonal networks of carbon stacked as layers. These stacked layers are held together by weak van der Waals bonds and can be easily broken unlike the hexagonal network. In the graphite structure, every carbon atom has three nearest carbon atoms in plane exhibiting $sp^2$-hybridization, as illustrated in **Figure 1**.

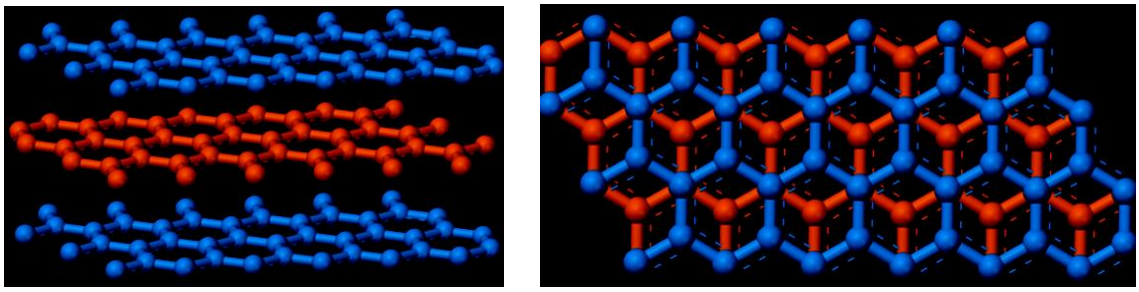

**(a)** **(b)**

**Figure.1. (a)** Side view of stacking and **(b)** plane view of stacking in graphite structure. Figure adapted from(*7*).

The search for carbon magnetism has gained further momentum with the discovery of newer allotropes of carbon such as fullerenes, carbon nanotubes, glassy carbon, carbon nanofoams and nanoribbons.(8) Currently there are over 100 research articles and more than 30 patents on synthesis and applications of carbon based magnetism.(9) The advantages of developing such metal free all carbon magnetic systems are multifold. Besides biocompatibility and light weight magnetism, the other major advantages are the low costs of production and easy processing.

Graphite has been traditionally known to exhibit diamagnetic behavior. Diamagnetism is the phenomenon by which non-magnetic materials resist an externally applied magnetic field leading to repulsion. Three different mechanisms to realize graphite magnetism have been theoretically predicted. Among these, the introduction of structural defects of $sp^3$ nature disrupting the planar $sp^2$ graphite structure has been experimentally shown to induce magnetism corroborating with theoretical models.(10-14) Itinerant electron transfer within the lattice and negatively curved $sp^2$ hybridized domains in carbon structures are the other two factors observed to induce magnetism.(15,

16) Itinerant magnetism in graphite arises from the transfer of delocalized electrons within its crystal lattice. Although negatively curved domains are centers of magnetic ordering, they rarely occur in graphite structures making fundamental research arduous. Further, theoretical predictions indicate itinerant magnetism from strong electron-electron interactions in carbon based structures including graphite, but experimental proof to validate this claim is yet to be reported.(17, 18) Among the above three mentioned factors, the $sp^3$ defect promoted magnetism is the most researched and widely accepted mechanism in inducing magnetism in graphitic structures.

Experimental proof for the existence of magnetism in graphite has been dealt with skepticism primarily due low magnetization values, lack of reproducibility, difficulty in scaling up, presence of magnetic impurities and production of metal free macroscopic amounts of magnetic graphite.(19-21)

Despite numerous recent reports indicating magnetism in graphite prepared by different methods and validated using various techniques, the presence of metallic impurities has been a major concern.(10, 22) The observation of weak magnetism in the starting carbon sample prior to processing is the reason for this. While processing shows a multifold increase in magnetization in these carbon samples, the role of metallic impurities cannot be accounted for by simply subtracting out the magnetization values observed prior to the processing. This is better understood by describing the structural existence of a magnetic phase in non magnetic materials. Magnetic moments have been shown to persist as magnetic islands in a non-magnetic matrix.(23) The presence of metal impurities in the non-magnetic material may align nearby diamagnetic moments (magnetic moments that do not have a preferred alignment) towards ferromagnetic

ordering (most magnetic moments are aligned parallel to each other). Thus, by altering the alignment of moments along one direction, metallic impurities like iron can lead to magnified observations of magnetization in carbon materials. Further, the presence of even low concentrations of metallic impurities casts doubts on the origin of magnetism in carbon. In order to conclusively establish magnetism in graphite or any other carbon based material, the starting carbon samples must be characterized for magnetic signals prior to processing.

### 1.2. Critical Review of Current Literature on Graphite Magnetism

In this section, some of the current literature pertaining to defect induced magnetism in graphite are reviewed. Initially, published research involving artificially induced defects in graphite is discussed. These include primarily proton bombardment studies and implantation of atoms/ions. Later, magnetism at naturally occurring defect sites in graphite is examined. Further, theoretical models and corresponding predictions on graphite magnetism are presented.

Proton irradiation of graphite samples has been found to induce magnetic ordering.(11) Here, highly oriented pyrolytic graphite (HOPG), a high quality synthetic grade of graphite was used. The HOPG samples were glued on to silicon wafers and irradiated with a 2.25 MeV proton beam. Magnetic characterization following the irradiation process indicated ferromagnetic ordering at room temperature in graphite. The authors here addressed the issue of metallic impurities that might contribute to the magnetization values by probing the samples using Particle induced X-ray emission (PIXE). Being a very sensitive technique in determining the elemental composition of the

sample, PIXE results showed very low amounts (< 3μg/ gm of sample) of iron impurities present in the HOPG samples. Despite being one of the pioneering papers to acknowledge the presence of metallic impurities, no magnetization values for HOPG samples before irradiation were recorded. Besides quantification of metallic impurities, magnetic characterization of the starting HOPG samples could reveal the specific contribution of impurities towards the ferromagnetic ordering observed.

Further investigations on the specific spots on HOPG samples irradiated with protons were reported in efforts to better understand the magnetism observed.(24) Topological scans performed on the HOPG surface before and after proton irradiation showed a distinct swelling at the irradiated spots with defect height increasing with irradiation dosage. Magnetic force microscopy (MFM) images taken on the spots showed remnant magnetization in terms of phase shifts, after brief application of a magnetic field suggesting ferromagnetism in irradiated HOPG. The seminal contribution of this research work pertains to the study of the topological defects in relation to the origin of magnetic ordering in HOPG. To determine if topological defects were sufficient in inducing magnetism, helium ions were bombarded on to the HOPG samples creating similar defect spots. MFM signals indicated almost negligible phase shifts and thereby the absence of magnetism. Proton implantation induces carbon bonding with hydrogen, creating $sp^3$ carbon. As mentioned earlier, the combination of $sp^2/sp^3$ carbon atoms exhibit magnetism, as observed in proton irradiated HOPG.(12, 21, 25, 26) Thus, hydrogen may play a crucial role in the origin of magnetism in carbon based structures and topological defects may not be entirely sufficient in promoting strong magnetization in carbon structures.

Individual evidence citing the important role of implanting a reactive species like hydrogen, nitrogen or even carbon on graphite and carbon based materials have been reported.(27) Here $^{15}N$ and $^{12}C$ ions were implanted on to nanoscale diamond particles. $^{15}N$ ions were found to induce greater magnetization in the carbon structures. Combining these results with the previously described implantations of hydrogen and helium, the origin of magnetism observed and rationale behind using a reactive species as compared to an inert element like helium were understood. Once the defects or vacancies in carbon structures are created by irradiation, the reactive species bind to these defect sites and prevent recombination between vacancies. This ensures that the defects are not diluted away and stabilizes the induced magnetic state.

Apart from irradiating graphite samples, a controlled etching process on graphite has been reported to induce magnetism.(28) In brief, the process involves a redox reaction on graphite in a nitrogen environment in the presence of copper oxide. Graphite samples processed by this method were reported to be ferromagnetic at room temperatures.(9) Impurity analysis on the samples showed the presence of copper and iron impurities. The contribution of such impurities were theoretically calculated, but no magnetic characterization of the samples prior to etching nor the role of impurities in magnifying the true carbon magnetization values were reported. Although a novel method to induce magnetism is presented, the question of true carbon magnetism without any contribution from impurities remains to be addressed.

Edges and grain boundaries are commonly identified line defects naturally known to occur in graphite. Extensive knowledge through theoretical investigations and experimental evidence for such graphite edges exist.(13, 14, 29-33) The edges occur in

two distinct shapes: zigzag and armchair. Evidence points towards magnetic ordering only in zigzag structures even in pure graphite due to the presence of edge states.(29) Further, it was found that zigzag edge magnetism persists only at lower temperatures and not at room temperatures. Even the value of magnetization was low and such zigzag edges are very rarely found in graphite.(30) Thus, zigzag defects cannot induce observable macroscopic magnetization in graphite, but nevertheless provides strong evidence for carbon magnetism.

Next, the grain boundaries are inevitable line defects specific to HOPG, mainly due to its production process. Grain boundaries are defects distributed on a two dimensional plane, equidistantly as shown in **Figure 2**. From the figure, grain boundaries can be understood to be dependent on the separation between layers of graphite. Here the filled circles and plain circles represent the two sublattices A and B. Defects in sublattice A and B have magnetic moments with opposing alignments. Only an unequal distribution of defects across the two sublattices can lead to a net magnetic moment in the graphite samples, as described by the widely accepted Hubbard's model for graphite magnetism.(13, 34, 35)

Magnetic characterization of grain boundaries provided experimental evidence for low magnetization values exhibited. Regardless of the irregularity in occurrence and the low magnetization values they confer on graphite, grain boundaries are significant proof for the existence of carbon based magnetism.

In order to explain electronic structure of induced magnetic states in graphite and theoretically calculate the associated magnetization values, density functional theory (DFT) studies have been carried out. DFT is purely a quantum mechanical approach,

popularly employed in physics and chemistry to evaluate the distributions of electronic densities.(36, 37)

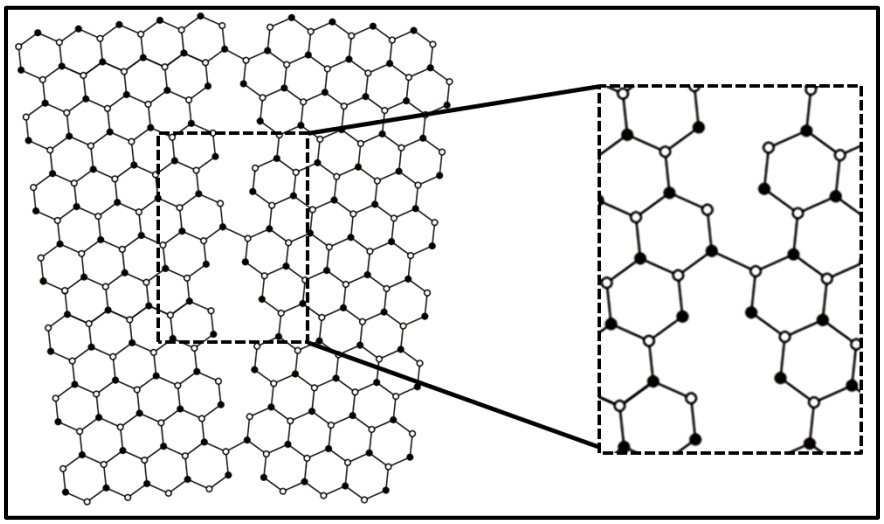

**Figure.2.** Grain boundaries observed in Graphite. Figure adapted from (16).

DFT studies explicitly predict magnetic ordering in proton irradiated graphite. Both hydrogen and helium irradiations produce defects that upon relaxation leads to a weak covalent bond formation between two neighboring carbon atoms.(38) This deforms the original hexagonal structure to a pentagon like structure observed in **Figure 3 (a)**, with new bond formation in carbon atoms labeled 1 and 2.(12, 39) The figure is an overlap of the graphite structure and the distribution of electronic densities (electron cloud). The vacancy created around carbon atoms labeled 1,2 and 3 have been calculated to have a net magnetic moment of about 1 $\mu_B$ (where is the $\mu_B$ is the Bohr magneton constant for an electron's magnetic moment) with all three carbon atoms having exactly one free bond, commonly referred to as $sp^2$ dangling bonds. The pentagonal structure saturates two of the three dangling bonds and the one remaining unsaturated dangling

bond is responsible for the net magnetic moment observed. Sometimes inter layer interactions among vacancies can lead to bond saturation resulting in no net magnetic moment.(26, 40, 41) Thus, magnetic ordering in defect induced graphite originates from unsaturated dangling $sp^2$ bonds as shown from DFT studies.

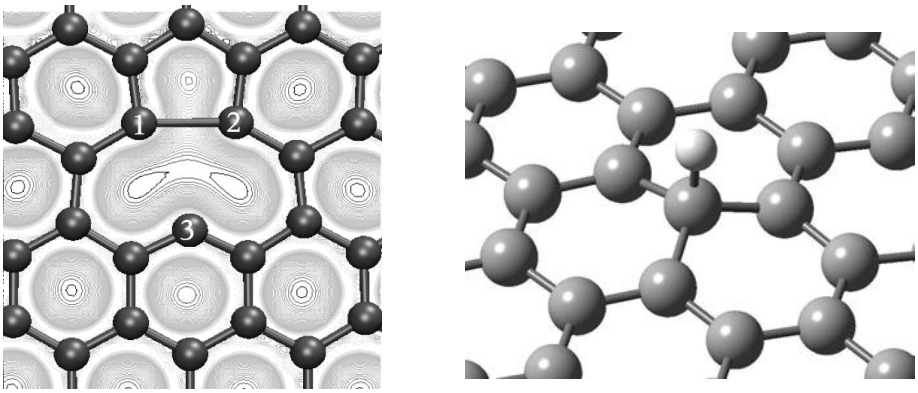


**(a)** **(b)**

**Figure.3.** Modifications in graphite structure either as **(a)** missing carbon atoms or **(b)** adsorption of hydrogen onto carbon atoms, as a consequence of proton irradiations. Figures adapted from (12, 33).

DFT studies have also predicted the possibility of hydrogen atoms adsorbed on to the surface of graphite referred to as adatoms to induce magnetic ordering.(12, 13, 33, 42, 43) As with the case of hydrogen bonding at defect sites, the adatoms also attach to carbon by breaking its $\pi$ conjugation. As shown in **Figure 3 (b)**, the adsorbed hydrogen atoms displaces both the attached carbon atom and to a small extent the nearby carbon atoms.(44, 45) Such hydrogen adsorptions are frequent events as a consequence of hydrogen irradiation. Theoretical evaluations indicate the absence of unsaturated dangling $sp^2$ bonds in case of such hydrogen adatoms and present a net magnetic moment

of about 1 $\mu_B$ as well. Thus, hydrogen adatoms are evidence of graphite magnetism even in the absence of previously described dangling bonds.

From above mentioned DFT studies, hydrogen induced graphite magnetism initially exhibit metastable magnetic moments around 2.3 $\mu_B$ but later reduces to a stable value in the range of 0.9 – 1.3 $\mu_B$ per hydrogen. The corresponding measured magnetization values reported for hydrogen irradiated graphite are very low, typically in the range of $10^{-4}$ to $10^{-6}$ emu.(16, 19, 24) With evidence showing higher magnetization values, backed by the robust theoretical calculations mentioned earlier, macroscopic levels of graphite magnetism can be established.

### 1.3. Graphite Magnetism: Issues to be addressed

In the search for novel methods to induce higher values of magnetization, two key questions yet to be addressed in the field of carbon magnetism in general and specifically for graphite are as follows:

1. Only ferromagnetic ordering has been observed in graphite. As defects can be controlled and tailor made, can magnetism be tuned? In other words, can different magnetic states like paramagnetism or superparamagnetism be induced in graphite? From a biomedical imaging standpoint, paramagnetic and superparamagnetic materials are valuable resources for minimally invasive diagnostics.

2. Can macroscopic amounts of magnetic graphite be produced? Large scale production of magnetic graphite in a repeatable process would decisively prove the phenomenon of carbon magnetism.

### 1.4. Potential Application- Magnetic Resonance Imaging Contrast Agent

Over the past three decades, medical imaging techniques have offered doctors and researchers the ability to examine what is happening inside the human body in a non-invasive manner. MRI is one among the very few prominent imaging techniques that have revolutionized this field. Published research estimates the market for MRI scanners by 2012 to be $2.8 billion in the US only, making it the fastest growing (compounded annual growth of 9.8%) among all imaging equipments.(46) Today over 70 million MRI scans are performed annually across the world, employing a little over 25,000 MRI scanners.

#### 1.4.1. Fundamentals and Background of MRI

The fundamental principle underlying the MRI technique is nuclear magnetic resonance (NMR). First discovered in 1946, NMR is based on the finding that atoms respond to magnetic fields.(47, 48) The atomic nuclei have a spin angular momentum and in the presence of an applied magnetic field the nuclear spins are oriented along the field. As a consequence, these nuclear spins behave as small magnets with a net magnetization. The MRI capitalizes on the fact that two-thirds of all the elements in the human body are hydrogen and produces images using the magnetic behavior of hydrogen atoms.

Under the influence of an applied magnetic field, all the hydrogen atoms align along the field as shown in **Figures 4 (a, b)**. A radiofrequency pulse applied orthogonally disturbs the orientation of the hydrogen atoms, illustrated in **Figure 4 (c)**. Once the RF is removed, the hydrogen atoms relax back aligning along the magnetic field, aided by the emission of more RF waves **(Figure 4 (d))**.(49, 50) The emitted RF waves are characteristic of the hydrogen milieu within the tissue.(51) The emitted radio waves differ between normal and affected regions within the tissue and results in differential relaxation of hydrogen atoms providing contrast for identifying the diseased tissue regions.

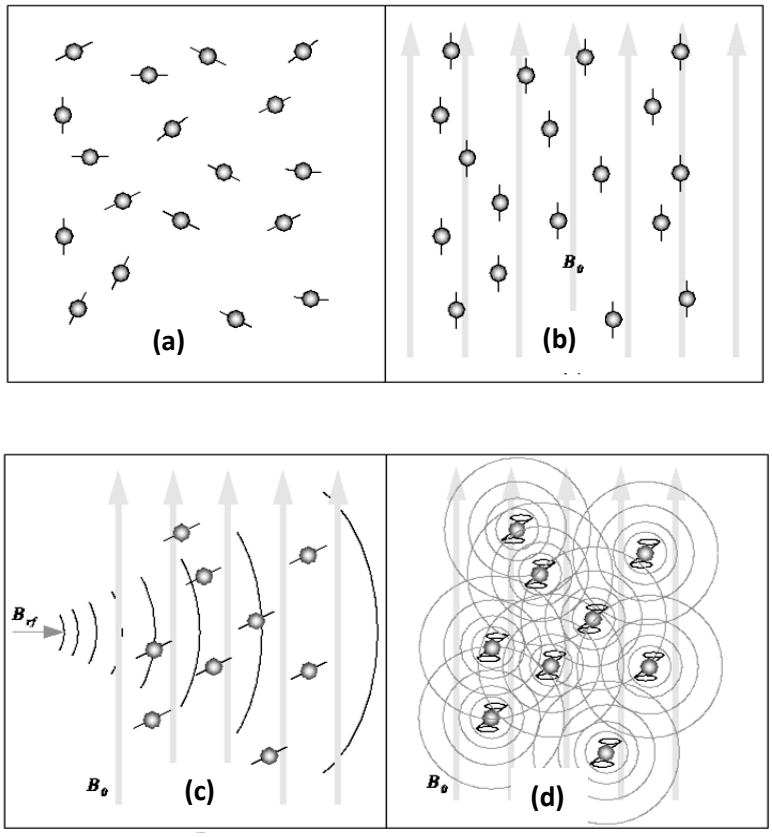


**Figure.4.** Nuclear spins orientation during magnetic resonance imaging. **(a)** Proton nuclear spins in tissue prior to application of an external magnetic field. **(b)** Nuclear spins

reach equilibrium by aligning along the direction of the applied field. **(c)** Application of an orthogonal RF pulse. **(d)** Relaxation of excited protons towards equilibrium orientation.(52)

The relaxation or the return of hydrogen atoms towards equilibrium by aligning along the applied magnetic field occurs through two mechanisms.(53) The applied radio waves impart excess energy to the hydrogen nuclei which relax by dissipating it as vibrations and rotations inside the lattice. This energy transfer from the nuclear spins to the surrounding lattice is termed as spin-lattice relaxation or also as longitudinal relaxation. The time for 63% recovery of magnetization after the applied radio pulse is referred to as T1. The RF pulse applied orthogonal to the magnetic field aligns the protons perpendicular to the field. The second mechanism of relaxation involves the dephasing of proton nuclei away from this perpendicular orientation towards equilibrium. This dephasing is effected by interactions between the spins and hence referred to as spin-spin relaxation. T2, also referred to as transverse relaxation time, denotes the time taken for the signal to regain 37% of its original signal.

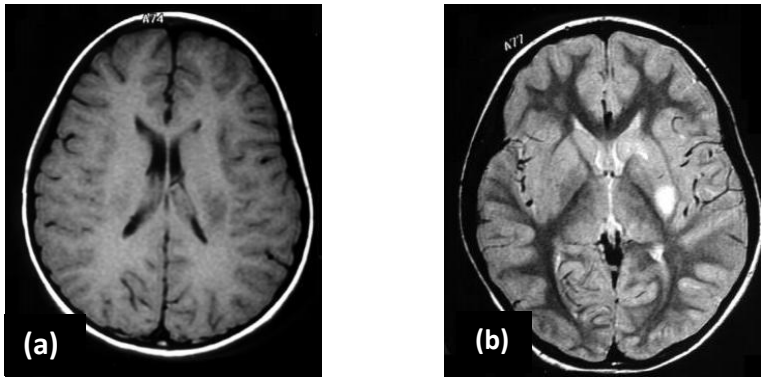


**Figure.5.** Image slices of brain from MRI recording **(a)** only T1 relaxation and **(b)** T2 relaxation.(54)

Most of MRI scans performed across the world capitalize on T1 relaxation, although in some cases where the contrast provided by T1 relaxation is insufficient, T2 relaxation is availed. **Figures 5 (a) and (b)** show MRI image slices of brain with contribution from T1 and T2 respectively.

MRI can distinguish almost all kinds of tissues and has the advantage of posing no health risk to patients making numerous scans possible. With almost no patient preparation and recovery time involved, MRI scans are the most sought after medical imaging procedure for diagnostic purposes.

### 1.4.2. MRI Contrast Agents

Magnetic materials that enhance the contrast between tissues (typically between healthy and affected tissues) in MRI images are known as contrast agents. This increase in contrast significantly improves the sensitivity and resolution of MRI scans. With enhanced accuracy, the MRI CAs help make better diagnosis. Today, more than 43% of MRI procedures involve the use of contrast agents.

A major goal of CA development is to increase the inherent relaxation potency of the agents. CAs used in clinical MRI procedures operates by changing (shortening) the relaxation times (T1 or T2) of water molecules in their vicinity. Paramagnetic contrast agents are composed of $Gd^{3+}$ ions and predominantly reduce the longitudinal relaxation times (T1). Clinically approved iron oxide nanoparticles containing contrast agents are superparamagnetic in nature and enhance contrast by significantly reducing the transverse relaxation times (T2). There are several types of MRI CAs. These include (ECF) agents,

extended-residence-intravascular agents (blood pool), and tissue (organ)-specific agents, molecular/cellular agents. The quantitative measure of efficacy is called relaxivity which is defined as change in relaxation rate of water per concentration of the CA and has units of mM-1s-1.

Among clinically approved contrast agents, gadolinium based ones find more prominent usage. The extracellular character of these contrast agents enables quick diffusion into the extracellular fluid space. One of the major drawbacks of these contrast agents are short intravascular retention periods in the order of 3 to 30 minutes, significantly limiting the time period for MRI data collection. The time between intravenous injection of the contrast agent and MRI scan must be optimized, to avoid substandard data quality. Thus, for vascular investigations large contrast agent dosages and rapid injection times are necessary. Due to toxic effects, MRI scanning protocols prohibit repeated administrations and limit the quantity of contrast agents. Although repeated imaging with low contrast agent doses could be implemented, a notable loss in signal strength is observed.(55, 56)

Ultra small superparamagnetic iron oxide (USPIO) and superparamagnetic iron oxide (SPIO) particles are two known T2 contrast agents.(57, 58) As particles, SPIO are taken up by the reticuloendothelial system. These remain intravascular for longer periods in the order of 1 to a few hours and can thus be employed as blood pool agents. The much smaller USPIO particles accumulate in the reticuloendothelial system much slower than the larger SPIO particles, thus resulting in longer plasma half-lives.(59)

As mentioned earlier, contrast agents are considered blood pool agents when longer time periods are required for elimination from the body. Such higher retention times increases the signal strength from blood enabling better diagnosis. Currently several mechanisms have been identified for their delayed elimination. One such mechanism involves reversible binding of the contrast agents with albumin, thus preventing the rapid passage of contrast agent into the interstitial spaces. (60-62)

Further, increasing the molecular size of contrast agent impedes their leakage across pores in the endothelium.(63-65) Typically contrast agents are eliminated through the kidneys and a change in the elimination process or the route involved can also cause longer retentions. Since larger concentrations of contrast agents are retained within the vascular regions, the required dosage is substantially lowered.

Magnetic resonance angiography (MRA) is a non-invasive imaging technique based on the principles of MRI and is used to specifically examine blood vessels. Recently, contrast enhanced MRA (CE-MRA) procedures are carried out more commonly with extracellular contrast agents.(66) One of the major drawbacks of commercially available contrast agents employed in CE-MRA is their low half lives, typically about 15 minutes. Slow data acquisition times of MRA systems further complicate the imaging procedure, limiting the time frame for imaging to less than 3 minutes. Hence, either non-toxic contrast agents enabling repeated imaging or intravascular blood pool agents hold the promise for better MRA data quality and accuracy.(67)

### 1.5. Rationale for Graphite Magnetism

Graphite, an allotropic form of graphite has been successfully used in biomedical applications as coatings for implants. Graphite biocompatibility has been demonstrated by in vivo studies with artificial cardiac valves and dental implants with no clot formation observed.(68-71) Further, no significant inflammatory response was observed in short term studies of graphite exposure to blood capillaries.(72) Osteoinduction properties of graphitic carbon coated on stainless steel substrates have been investigated in vitro.(73) Results indicate superior cellular adhesion and proliferation on graphitic coatings, providing additional evidence of its biocompatibility. Graphite biocompatibility has been established with studies investigating cell in growth and proliferation on pyrolytic graphite.(74)

Developing an organic magnetic material has numerous advantages from both a material science and medical imaging perspective. Graphite based magnetic materials would involve low costs of production along with easier processing. The idea of light weight magnetism is fascinating, with potential in novel applications in devices. In addition to the above mentioned advantages, biocompatibility of graphite makes them attractive candidates as contrast agents in medical imaging applications.

Graphite based contrast agents/ blood pool agents are ideal candidates for MRI and MRA imaging for the following reasons:

1. Graphite is biocompatible, non-inflammatory and less toxic in comparison to metal atoms that are present in clinically approved contrast agents. Hence, higher dosages and repeated imaging can be feasible.

2. Metal free graphite does not hold the risk of dissociation as in the case of contrast agents where metal atoms could escape from chelates leading to toxicity.
3. Micro-graphite particles used here are larger in size compared to molecular sizes of gadolinium and iron oxide nanoparticles based contrast agents. The larger size can significantly improve their half life in the extracellular and intravascular regions, thus improving the signal intensity and thereby the contrast in MRI and MR Angiography.
4. Graphite has been shown to bind human serum albumin in a reversible manner without denaturing the protein.(75, 76) As discussed earlier, contrast agents that can bind human serum albumin have longer retention times inside the human body and find applications as blood pool agents. Clinically used blood pool agents today are based on this mechanism of albumin binding to enhance retention times.(62, 77, 78)

### 1.6. Outline of Thesis

In order to realize the application of graphite as a contrast agent for MRI, inducing magnetic behavior in graphite is a prerequisite. Material characterization studies comprising particle size distribution, scanning electron microscopy imaging (SEM) and impurity analysis performed by Inductively coupled plasma Optical emission spectroscopy (ICP-OES) on micro-graphite particles are presented in the initial half of Chapter 2. Further, the novel chemical synthesis process developed to induce magnetism in graphite is elaborated.

To achieve magnetism in micro-graphite particles, defects are induced through the hydrogenation process developed here. In order to characterize the material for the presence of structural defects and for the formation of hydrogen bonds on graphite, Raman microscopy and Near edge X-ray absorption fine structures spectroscopy (NEXAFS) were performed respectively. In the presence of defects, the Raman spectrum of hydrogenated micro-graphite samples would indicate an increase in the disorder band suggestive of the presence of $sp^3$ defects. NEXAFS is an element sensitive technique and the presence of hydrogen bonds as well as the evidence for hydrogenation can be obtained from the NEXAFS spectra of hydrogenated micro-graphite particles. The results of the above mentioned structural characterization techniques performed on processed and pristine micro-graphite particles are presented in the latter parts of Chapter 2.

Next, to determine the magnetic behavior of hydrogenated micro-graphite particles in comparison to the unprocessed particles, Superconducting Quantum Interference Device (SQUID) measurements were performed. Magnetization values were recorded and the specific magnetism displayed by the micro-graphite particles at every step of the processing are presented towards the end of Chapter 2. Besides the SQUID analysis, relaxation rate measurements as function of magnetic field were carried out on processed micro-graphite particles. Relaxation rates help investigate the performance of contrast agents and are indicative of the mode of relaxation (T1 or T2) predominantly displayed. In order to visualize the contrast enhancing ability of hydrogenated micro-graphite particles, MRI phantom imaging was carried out alongside a commercially available contrast agent. The NMRd and MRI Phantom imaging results are discussed towards the end of Chapter 2 as well.

Magnetic micro-graphite particles developed here hold the promise as ideal replacements for commonly used contrast agents with metal ion chelates. In-vitro Calcein AM viability studies were carried out in J774 murine macrophages in order to investigate the biocompatibility of micro-graphite particles relative to metal atoms commonly used in contrast agents (Iron, Gadolinium and Manganese). The results of this in-vitro study are presented in Chapter 3. All the results have been summarized and a future perspective on the research efforts required to achieve clinical application of magnetic graphite based contrast agents are presented in Chapter 4.

## Chapter 2: Synthesis and Characterization of Magnetic Micro-Graphite

### 2.1. Micro-Graphite Particles

The starting graphite material used for the study is analytical grade micro-graphite (Catalogue number 496596, Sigma Aldrich) with a particle size of less than 45 microns referred to as pristine micro-graphite here. To characterize the pristine micro-graphite particles, scanning electron microscopy (SEM, JSM 5300, JEOL) was carried out at an electron beam voltage setting of 80kV. Size distribution of the micro-graphite particles was estimated to be around 24 micrometers using the ImageJ software (image processing and analysis software from NIH, USA).

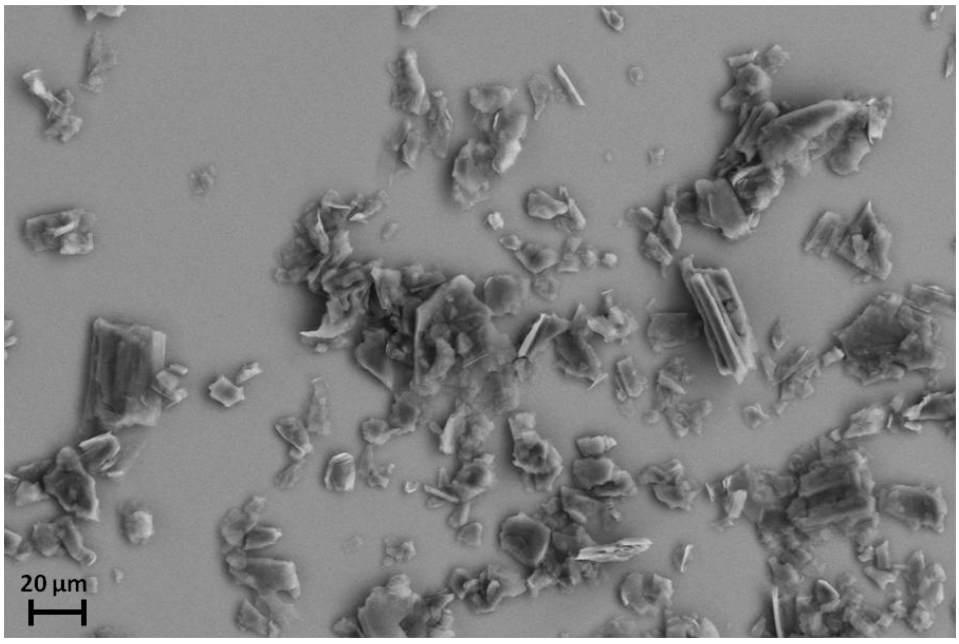


**Figure.6.** Scanning Electron Microscopy of pristine micro-graphite particles

## 2.2. Chemical Synthesis Protocol

Fluorination, the process of attachment of fluorine atoms was performed on the pristine micro-graphite samples at a private industrial establishment (Fluoro-seal International, L.L.P., Houston, Texas). Following a commonly followed literature method, the fluorinated micro-graphite samples were prepared in a quartz furnace maintained at an inert atmosphere. The micro-graphite particles were then exposed to 2% fluorine gas diluted in helium at an elevated temperature of about 325K. The reaction time was 2 hours for this fluorination process. The gaseous impurities in the fluorine gas, specifically hydrogen fluoride was filtered out using a hydrogen fluoride trap consisting of sodium fluoride pellets. The sample collected after the processing would be henceforth referred to as fluorinated micro-graphite.

The fluorinated micro-graphite samples of about 10 mg were then placed in quartz tubes in a Chemical Vapor Deposition (CVD) system (Easy Tube 2000 First Nano, Ronkonkoma, NY) to induce hydrogenation. Initially the samples were flushed with Argon gas at a rate of 2 liters/min to establish an inert atmosphere. The temperature inside the CVD system was gradually increased to 900° C and maintained at this elevated temperature for 45 minutes. Fluoro-carbons are produced as a result of this pyrolytic process. Defect sites were created due to the expulsion of fluoro-carbon species released from fluorinated micro-graphite samples.

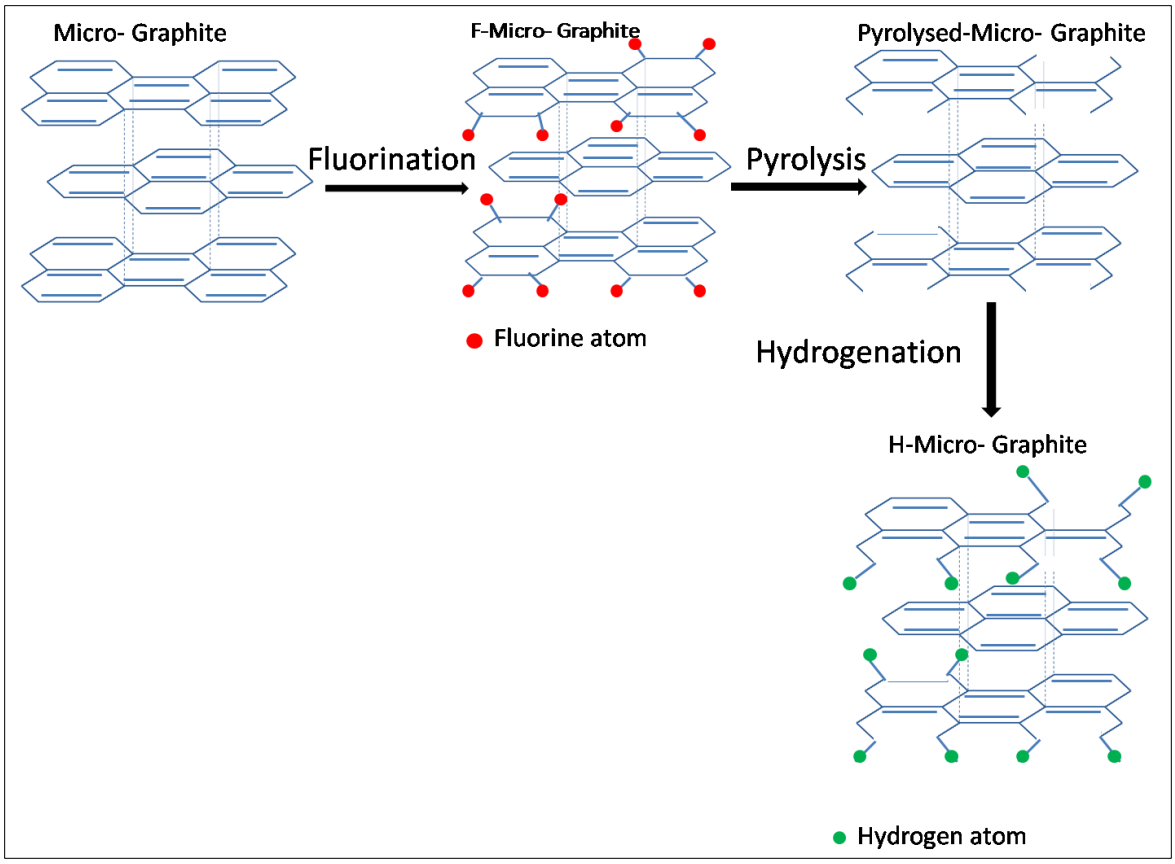


**Figure.7.** Schematic of CVD hydrogenation process to induce magnetism in graphite

The removal of such fluoro-carbon species is critical for the next step that involves hydrogenation. In order to facilitate this removal, the CVD chamber was purged with Argon at a rate 2 liters/min for 15 minutes. Following this argon flush, the hydrogenation of the defect sites in the pyrolyzed micro-graphite was initiated by passing hydrogen gas at a rate of 0.2 liters/min for 45 minutes keeping the CVD core temperature constant at 900° C. Argon was purged at 2 liters/min to gradually lower the CVD core temperature to about 200° C to facilitate sample removal post hydrogenation. A total

processing time of about 2 hours was required at the CVD system to produce hydrogenated micro-graphite with almost no loss of sample.

### 2.3. Metal Impurity Analysis

Metallic impurities present in carbonaceous materials might contribute to the magnetism of carbonaceous material. As a false positive magnetic signal, metallic impurities could undermine the claim of magnetism in organic materials. To address this concern, Inductively-coupled plasma optical emission spectroscopy (ICP-OES) was used to analyze pristine micro-graphite samples for the presence of such impurities. ICP-OES is a spectroscopic technique commonly used for trace element analysis. The plasma excites the atoms in the sample material which emit characteristic electromagnetic waves specific to the elements present, making it a very sensitive technique.

The specific metals that were analyzed for were iron, cobalt, nickel, chromium, copper and manganese, which are metals identified to exhibit magnetism. **Table.1** carries results obtained from a private micro-analytical laboratory (Columbia Analytical Services, Tucson, AZ).

**Table.1.** ICP-OES analysis of magnetic elements in the graphitic structures known contribute to its magnetic properties. ($^{\#}$ refers to the detection limit of the particular element by ICP-OES)

| Element | Concentration (wt%) |
|---|---|
| Cobalt | $<0.006^{\#}$ |
| Chromium | $<0.006^{\#}$ |
| Copper | $<0.006^{\#}$ |
| Iron | $<0.01^{\#}$ |
| Manganese | $<0.006^{\#}$ |
| Nickel | $<0.006^{\#}$ |

**Structural Characterization**

Two very sensitive techniques, Confocal Raman Microscopy and Near Edge X-ray Absorption Fine Structures spectroscopy were performed on pristine micro-graphite particles and their hydrogenated counterparts. Combining results from these two studies, structural defects, specific elements involved in the defects and the coordination of these elements can be inferred. Initially, the $sp^3$ structural defects produced by the hydrogenation process and then presence of hydrogen bonds created thereby were evaluated qualitatively using the above mentioned methods.

## 2.4. Raman Spectroscopy

Raman spectroscopy is an analytical technique where the light scattering property of the sample is exploited to characterize the molecular structures, chemical bonding and

how these are affected as the sample experiences stress or undergoes processing. A monochromatic light source, typically a laser is used and the shift in energy of the scattered light collected gives information about the rotational, vibrational and other phonon modes in the sample.

### 2.4.1. Instrumentation and Sample Preparation

Raman spectroscopy was carried out using the WITec Alpha Confocal Raman Microscope (WITec Instruments Corp., Maryville, TN). The Raman spectra were collected with a 532 nm excitation laser source (n=4). The samples, pristine micro-graphite, fluorinated micro-graphite and hydrogenated micro-graphite were dissolved in 500µl of acetone and dip coated on to glass slides under clean room conditions.

### 2.4.2. Results and Discussion

The Raman spectra for pristine micro-graphite and hydrogenated micro-graphite are shown in **Figure 8 (a-c)** respectively. The spectra for all three samples have a prominent G band (graphite band) at 1580 $cm^{-1}$, characteristic of graphite.(79) The D band (disorder band) at 1350 $cm^{-1}$ is significantly different for the three samples, progressively increasing with processing. For pristine micro-graphite the peak height for the D band is extremely small, indicating almost lack of any possible defects.(11, 80) The D band for fluorinated micro-graphite shows an increase in peak height compared to that of pristine micro-graphite. This increase in D band peak height is expected as the fluorination process produces C-F bonds altering the graphite environment.

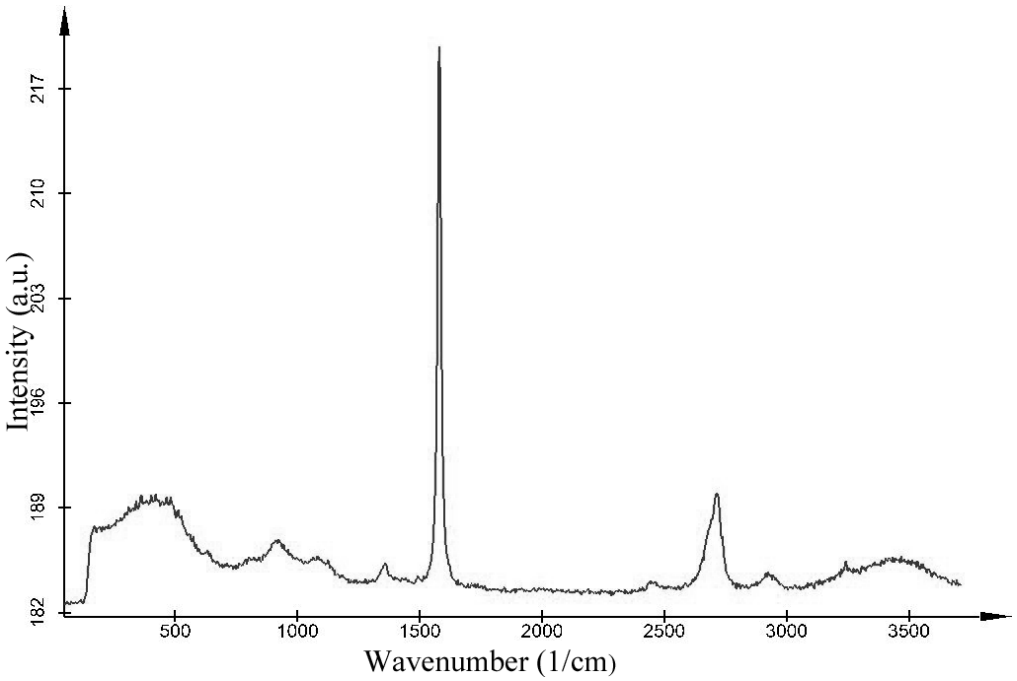


**Figure.8.a.** Raman Spectra at 532 nm for pristine micro-graphite particles.

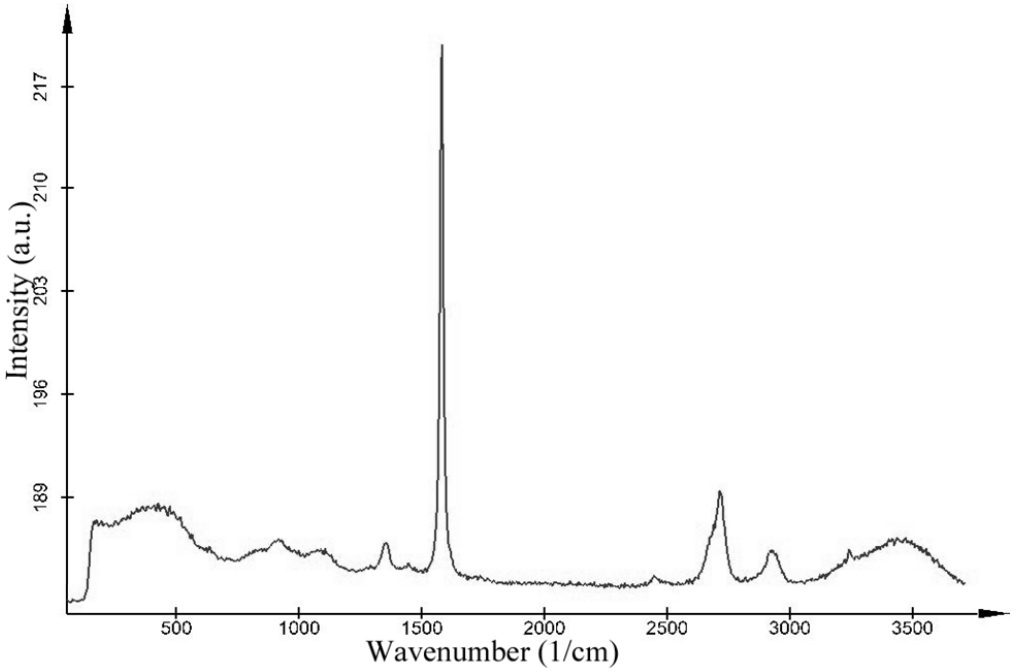


**Figure.8. b.** Raman Spectra at 532nm for fluorinated micro-graphite particles

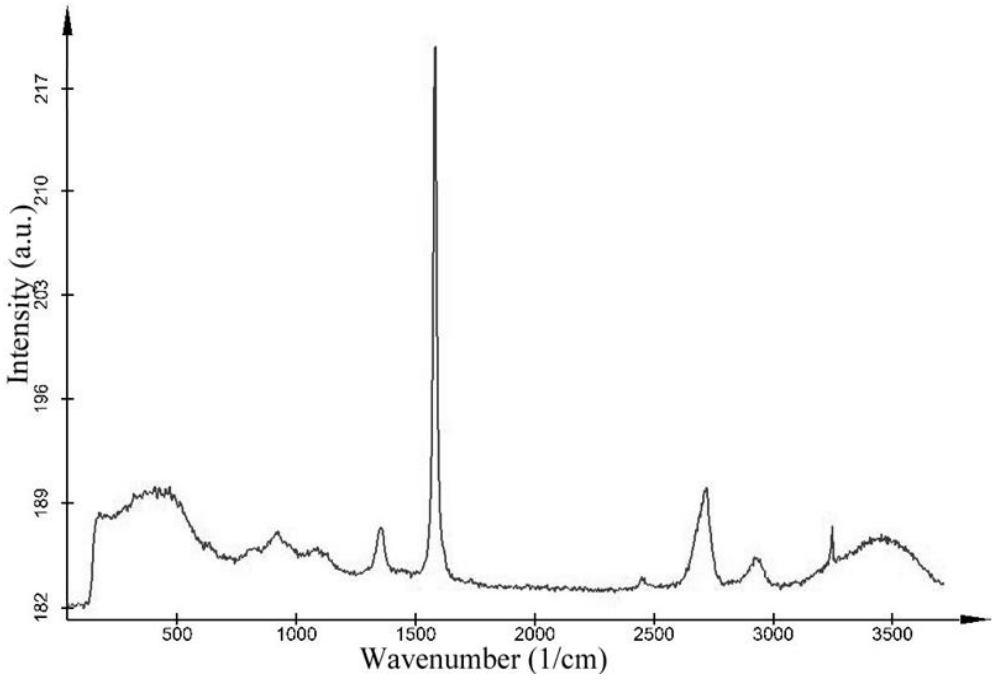


**Figure.8. c.** Raman Spectra at 532nm for hydrogenated micro-graphite particles

The pyrolysis process followed by hydrogenation to produce hydrogenated micro-graphite is expected to induce more defects to the graphite structure and is believed to produce dangling hydrogen bonds from sites of fluorination, increasing disorder in the structure. As anticipated in the case of hydrogenated micro-graphite, the characteristic D band at 1350 cm-1 is more prominent compared to the other two samples. This indicates a significant increase in the number of defects as a consequence of the processing at each step. The G bands of all the three samples show that there is no increase in height or broadening or of the peak at 1580 cm-1. This information establishes the fact that the graphitic structure is intact even after the various steps of processing. In Figures 8 (a-c), peaks are observed at wavenumbers higher than 2000 $cm^{-1}$. These peaks are overtones of the G and D band explained earlier. Although they indicate the presence of graphitic

structures and presence of defects, the sensitivity of the structural information these signals provide are lesser than the peaks observed below 2000 $cm^{-1}$.

The above results establish that the various steps of processing i.e. fluorination, pyrolysis and hydrogenation of the micro-graphite sample do not destroy the graphitic structure but induces defects increasingly.

### 2.5. Near Edge X-Ray Absorption Fine Structure Spectroscopy (NEXAFS)

NEXAFS is a spectroscopic method widely used in materials research to probe the bonding milieu of samples in the study oxidative states of metals, magnetic, biological and polymeric materials. Here soft x-rays typically below 1000 eV of photon energy are scanned onto the specimen and the x-ray intensity absorbed is computed.(81) Synchrotrons serve as ideal source for soft x-rays for scanning the samples.

Transmission and electron yield are two most widely used modes of NEXAFS operation. Here the electron yield mode is employed where the sample is grounded to an ammeter and the current used to neutralize is measured. In brief, the absorption of x-rays by an atom in the core of the specimen excites an electron to occupy a higher energy vacant state. The electron hole thus produced is filled by electron capture from a different shell accompanied by the emission of a photoelectron. When the energy levels of the excitation source resonantly matches that of the core atom level in the sample, characteristics peaks occur in the NEXAFS spectra making the technique very sensitive to minor changes in bonding states, length and angle.

### 2.5.1. Instrumentation and Sample Preparation

NEXAFS spectra for pristine micro-graphite, fluorinated micro-graphite and hydrogenated micro-graphite samples were measured at the U7A beamline at National Synchrotron Light Source (NSLS), Upton, NY. All the above mentioned micro-graphite samples were prepared by coating them onto silicon wafers using a spin coater. These spin coated wafers were then mounted to measure the NEXAFS spectra (n=4). A beamline monochromator with 600 lines/mm grating was used for scanning. An entrance grid voltage (EGV) of -50V dc was set to measure the partial electron yield. All data were normalized by drain current of an Au mesh ($I_0$).

### 2.5.2. Results and Discussion

To gain an understanding of how the processing alters the bonding properties in micro-graphite, the pristine micro-graphite and hydrogenated micro-graphite samples were characterized by soft x-rays-based NEXAFS, a very powerful analytical technique used to probe elements bound to carbonaceous samples. **Figure 9** shows the carbon K-edge obtained from hydrogenated micro-graphite and pristine micro-graphite samples, respectively. For normalization the drain current of an Au mesh ($I_0$) was used and all the data are vertically offset for clarity.

The NEXAFS spectra of hydrogenated and pristine micro-graphite samples show characteristic peaks at 285.6eV and 291.6eV specific to the C 1s to π* transition in the carbon double bond (C=C), and the C 1s to σ* transition of carbon- carbon single bond (C-C) found in the graphite structure, respectively.(82) Despite the similarities, the

NEXAFS spectra of hydrogenated micro-graphite sample shows a characteristic peak at 287.9eV, specific to the C 1s to σ* transition of carbon hydrogen sigma bond (C-H).(83) It is widely accepted that the hydrogenation process involving the reaction of molecular hydrogen on micro-graphite under the conditions previously elaborated is thermo-chemically unfavorable for the production of byproducts like methane or other hydrocarbons. Hence, the hydrogen bond formation that is observed from the NEXAFS spectra can be concluded to be occurring at the defect sites on micro-graphite only.

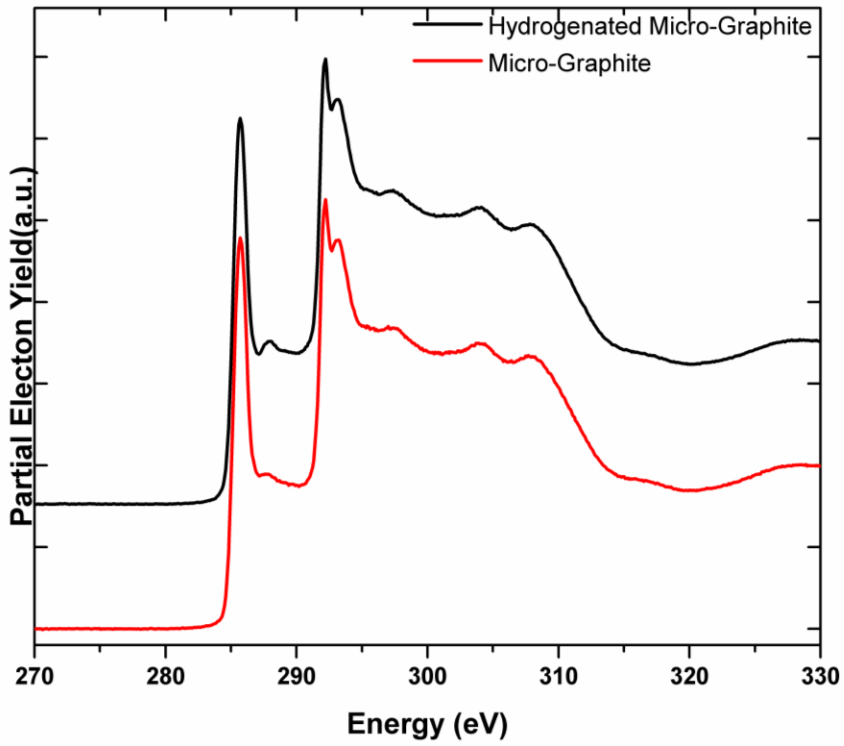


**Figure.9.** Near edge X-ray absorption fine structure spectra of pristine (red) and hydrogenated micro-graphite (black) obtained at partial electron yield with an entrance grid voltage (EGV) of -50V dc. Peak at 285.6eV, 291.6eV and 287.9eV represent C=C, C-C and C-H bonds respectively. Data offset for clarity.

The Raman and NEXAFS results taken together indicate that pyrolysis induces defects at the fluorinated sites on the micro-graphite with dangling carbon bonds, and the in situ hydrogenation enables bonding of hydrogen to at least a fraction of these carbon bonds at the defect sites.

## Magnetic Characterization

### 2.6. SQUID (Superconducting Quantum Interference Device) Characterization

The novel hydrogenation induced magnetism in graphite approach adopted here requires validation both in terms of its magnetic behavior and strength. Besides providing evidence for graphite magnetism, a better understanding of the underlying mechanism can be achieved by evaluating each of the processing steps involved. Hence, Superconducting quantum interference device (SQUID) measurements were performed on micro-graphite samples and the results are critically analyzed in great detail. Further the performance of the magnetized micro-graphite particles in terms of relaxation times and contrast enhancement were evaluated using Nuclear Magnetic Relaxation dispersion and MRI Phantom imaging, respectively.

#### 2.6.1. Introduction

SQUID (Superconducting Quantum Interference Device) magnetometry is one among the most sensitive techniques used for the measurement of very low magnetic fields. SQUID magnetometers have been employed to measure low magnetic fields generated in living organism, for e.g. in the rat brain. To put things in perspective, the

magnetic field generated in a rat brain is about $10^{-13}$ T and the lowest signal that a SQUID device could reliably record is in the order of $10^{-14}$ T. Apart from sensitivity, SQUID also provides for magnetic characterization of materials under externally applied magnetic fields in the order of a few Tesla across a wide range of temperatures, making it a very powerful analytical device.

The SQUID system can be operated under both DC and AC conditions, thus facilitating measurements of magnetization and magnetic susceptibility of the material respectively. DC magnetic fields can be employed to study the variation of magnetization of the sample as a function of both temperature (0-300K) and applied magnetic field (-6 to 6 Tesla). Further, the variation of magnetic susceptibility with temperature and magnetic field can be measured with an AC magnetic field.(84) This magnetometer setup comprises of two Josephson junctions in parallel constructed by a couple of superconductors disconnected by thin layers of insulating material, shown in **Figure 10 (a)**.

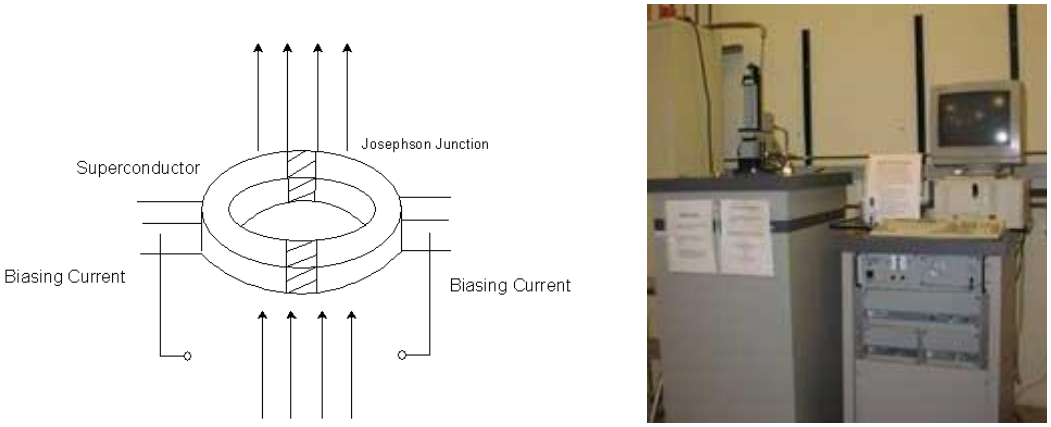


**(a)** **(b)**

**Figure.10.** Superconducting Quantum Interference Device **(a)** a simple SQUID set up, **(b)** SQUID magnetometer

In brief, the main components are as follows: (a) superconducting magnet, (b) a detection coil connected to the SQUID and (c) a magnetic shield. Due to its very high sensitivity, a magnetic shield is required to filter out fluctuations in the ambient magnetic field.

The magnetization measurements are carried out by moving the sample across the loop constructed with the Josephson junctions. In the case where the sample possesses a magnetic moment, it would perturb the magnetic flux across the loop. This in turn induces an electric current in the loop (the detection circuit consisting of the Josephson junctions), altering the existing current flowing through. This change in current flowing through produces a change in the voltage across the loop corresponding to the magnetization of the sample. In brief, the SQUID system acts as a current to voltage converter responding even to small fractions of the flux quantum, conferring it the very high sensitivity.

### 2.6.2. Sample Preparation and Instrumentation

All micro-graphite samples were weighed and loaded on to standard gelatin capsules. The use of paraffin to dissolve the micro-graphite samples prior to loading in gelatin capsules was avoided to be able to extract out the sample for reuse after SQUID analysis and also to reduce the background magnetic signal. The capsules have a background signal of $10^{-6}$ emu, which was subtracted out of all SQUID measurements. All sample handling were carried out under clean room conditions, taking care against any metallic contamination.

The magnetization of the micro-graphite samples were characterized using a SQUID system with a sensitivity of about $10^{-8}$ emu. SQUID analysis were carried out by varying the applied magnetic field from -50000 Oe to 50000 Oe (5T) over a temperature range of 0 – 300 K. Using the SQUID system, the variation of magnetization in the sample as a function of applied field and temperature were studied. For the variation of magnetization with the applied magnetic field studies, SQUID measurements were recorded for the following temperatures: 10 K, 150 K and 300 K over the entire range of applied fields mentioned above.

For the magnetization measurements as a function of temperature, studies were carried out in two different modes: (a) Field cooling and (b) Zero Field cooling. Here data were recorded over the temperature range of 0 to 300 K with a constant applied field of 500 Oe known as the coercive field. All readings were normalized to the mass of the sample. In the Field cooling (FC) method, a magnetic field is applied above a particular temperature and cooled down to low temperatures keeping the field constant. Here the magnetization is measured for the entire range of temperatures. In the Zero Field cooling (ZFC) mode, the sample is cooled in the absence of an applied magnetic field. Once the sample is cooled down to a specific temperature, the field is applied. Under the constant field, the sample is heated and the magnetization is recorded.

### 2.6.3. Results and Discussion

**Figure 11 (a-d)** shows the plot of magnetic moment (M) as a function of the applied field (H) for hydrogenated micro-graphite, pristine micro-graphite, fluorinated micro-graphite and de-fluorinated micro-graphite respectively (n=4). The M *vs.* H plot

for hydrogenated micro-graphite shows the existence of a hysteresis loop at 10 K, seen in **Figure 11 (a) insert**. The presence of the hysteresis loop with a residual magnetization of 200 Oe at zero applied magnetic field, points to the fact that the sample is magnetic and displays a magnetic state with ferromagnetic ordering. This value of residual magnetization of the sample is referred to as the coercive field. At higher temperatures, as observed at 150 K and 300 K, the magnetic moment plot shows a ferromagnetism-like behavior, but with zero coercive field and absence of the hysteresis loop. This suggests to a transition in the magnetic state of hydrogenated micro-graphite samples from ferromagnetic ordering towards superparamagnetism. However, the magnetization profile has a negative slope in the ranges of 10,000 Oe to 40,000 Oe, and between -10,000 Oe and -40,000 Oe. The negative slope suggests a decrease in the value of magnetic moments with increase in applied magnetic field, characteristic of diamagnetic behavior of the samples. Thus, hydrogenated micro-graphite exhibits a combination of ferromagnetic and diamagnetic signals at low temperature (10K) and indicates the presence of superparamagnetic and diamagnetic signals at higher temperatures (150 K and 300 K). The hydrogenation processing may not have evenly treated the micro-graphite samples, leaving a fraction of the sample non-magnetic (diamagnetic). This may significantly contribute to the diamagnetic portion of the magnetic signal, as seen in the plot.

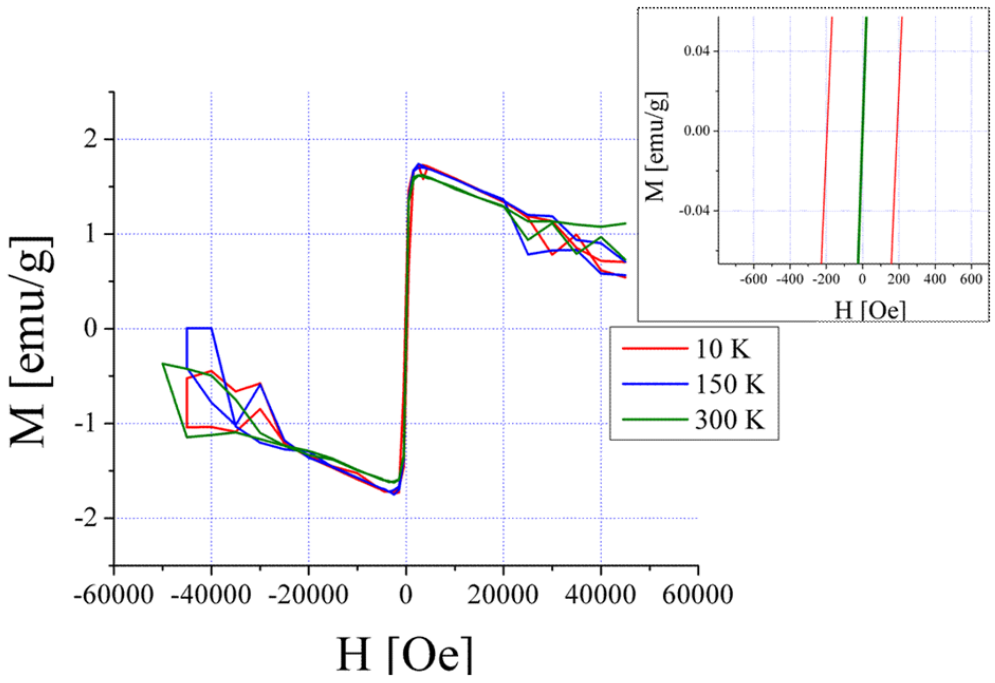


**Figure.11.a.** Magnetization versus applied field plot for hydrogenated micro-graphite showing superparamagnetic ordering at 10K (shown in insert) and ferromagnetic ordering at higher temperatures

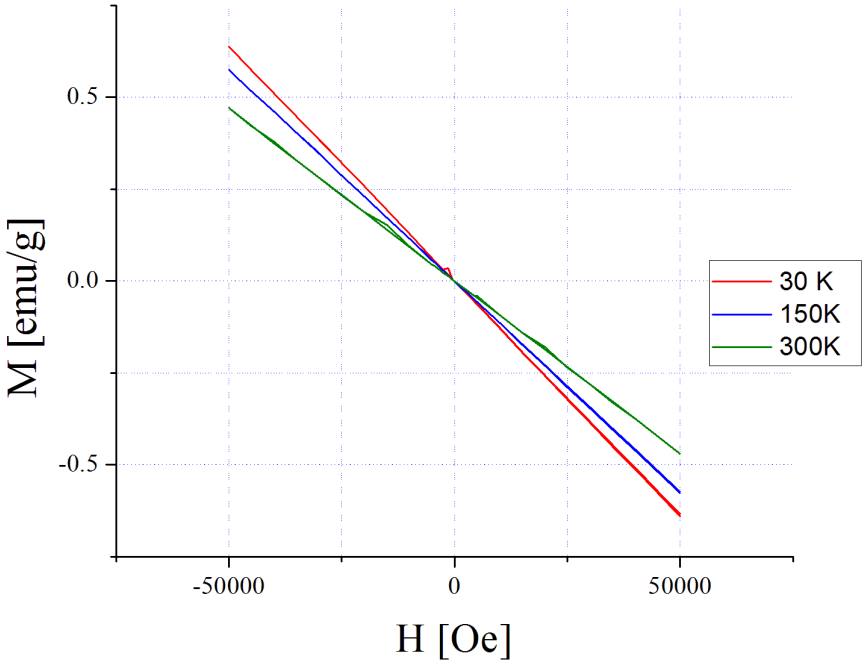


**Figure.11.b.** Magnetization versus applied field plot for pristine micro-graphite indicating non-magnetic behavior

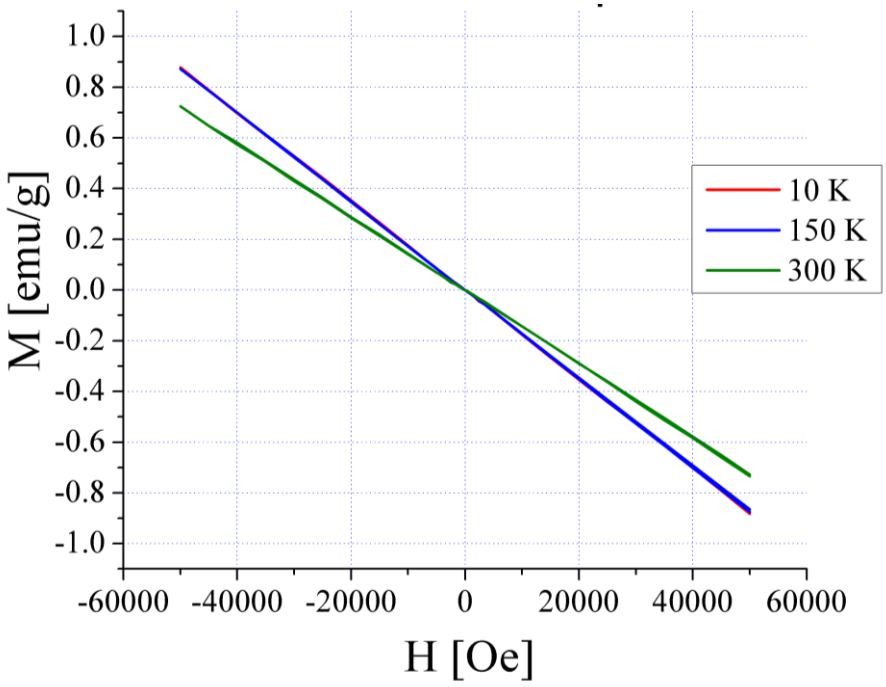


**Figure.11.c.** Magnetization versus applied field plot of fluorinated micro-graphite particles indicating non-magnetic behavior

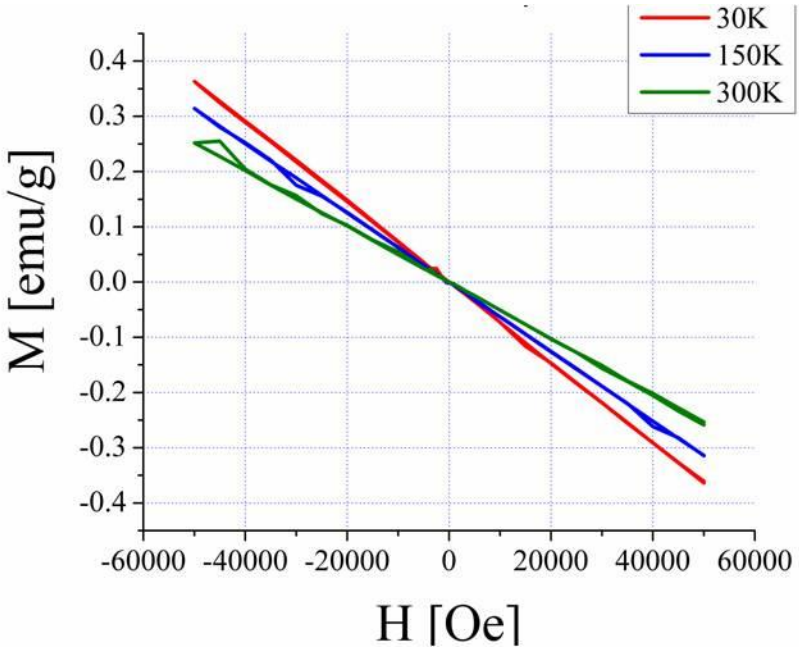


**Figure.11.d.** Magnetization versus applied field plot of pyrolyzed or de-fluorinated micro-graphite particles indicating non-magnetic behavior

**Figure.11.** Magnetization as a function of applied magnetic field by varying the applied fields from -5000 Oe to 5000 Oe at 298K for **(a)** Hydrogenated micro-graphite (insert shows the hysteresis loop and the coercive field), **(b)** pristine micro-graphite, **(c)** fluorinated micro-graphite and **(d)** de-fluorinated Graphite.

To gain a greater understanding into how the hydrogenation process induces magnetism, SQUID analysis were performed on micro-graphite samples at every processing step starting from the pristine samples. Magnetization plots **Figures 11 (b-d)** for pristine micro-graphite (starting material), fluorinated micro-graphite (first processing step), de-fluorinated micro-graphite (second processing step in CVD without hydrogen flush) show a diamagnetic ordering in the samples. This indicates the absence of magnetism in all the samples and highlights the importance of the hydrogen flush during CVD processing in inducing magnetism in graphite.

Theoretical studies suggest that a partial change in the $sp^2$ planar structure upon fluorination leading to a mixture of $sp^2/sp^3$ hybridization in graphite lead to magnetic ordering. Density functional studies on graphite systems with induced defect sites also indicate the presence of magnetic ordering.(12-14, 33) Defect sites are induced in the de-fluorinated micro-graphite samples when fluorinated samples are heated to about 1200 K in the CVD system. However, these samples do not show magnetism. This may be due to the fact that either the defect sites may have annealed when the samples were removed from the CVD system or the defects were not enough to induce a macroscopic measurable magnetism.

One of the most important concerns with developing organic magnetic materials is the presence of metallic impurities and their contribution towards the magnetic signal. As mentioned earlier in this chapter, the metallic impurities were either very low or well below the sensitivity of the ICP-OES apparatus. The magnetization plots of all micro-graphite samples excluding the hydrogenated samples encompass the entire treatment process and sample handling. The absence of magnetism in these samples suggests that the processing does not add magnetic impurities to the samples. Combining the impurity analysis data with the magnetization plots, it can be concluded that the origin of magnetism is due to the hydrogenation process and not due to any contamination by metallic impurities.

In recent studies, where ion implantation has been adopted to induce magnetism in graphite, SQUID data on the starting material prior to implantation shows magnetic ordering.(9, 28, 85, 86) This value of magnetic moment is subtracted from the signal produced by ion implanted graphite samples. Although such data suggest the possibility of magnetism in all carbon based structures, it does cast doubts on the role of magnetic impurities. Here, the pristine micro-graphite samples show absence of magnetism, thus providing concrete evidence for carbon magnetism.

Transition in magnetic states occurs when the magnetic moments are perturbed. With increase in temperature, the increase in thermal energy perturbs the magnetic moments. To validate the presence of more than one magnetic state and its transition at higher temperatures in hydrogenated micro-graphite, the variation of magnetization was plotted as a function of temperature in both FC and ZFC modes. **Figure 12 (a-c)** shows

FC and ZFC plots for hydrogenated micro-graphite, fluorinated micro-graphite and pristine micro-graphite, respectively. If the sample under examination possesses only one magnetic state independent of temperature, the ZFC and FC curves overlap. In **Figure 12 (a),** the ZFC and FC profiles are distinct and do not overlap, suggesting the presence of more than one magnetic state in hydrogenated micro-graphite. The curves intersect at around 125 K, known as the blocking temperature ($T_B$) where the transition from one magnetic state to another materializes. The magnetization as a function of applied magnetic field plot for hydrogenated micro-graphite **Figure 11 (a)** combined with the blocking temperature data **Figure 12 (a)** provides evidence on magnetic states and its transition.

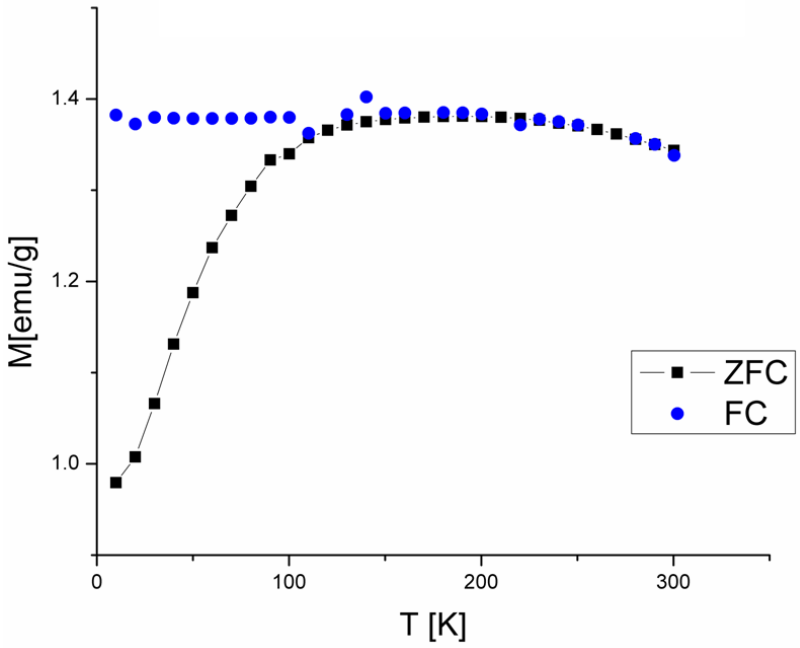


**Figure.12.a.** Magnetization versus temperature plots for hydrogenated micro-graphite over 5-300K with an applied field of 500 Oe at FC conditions.

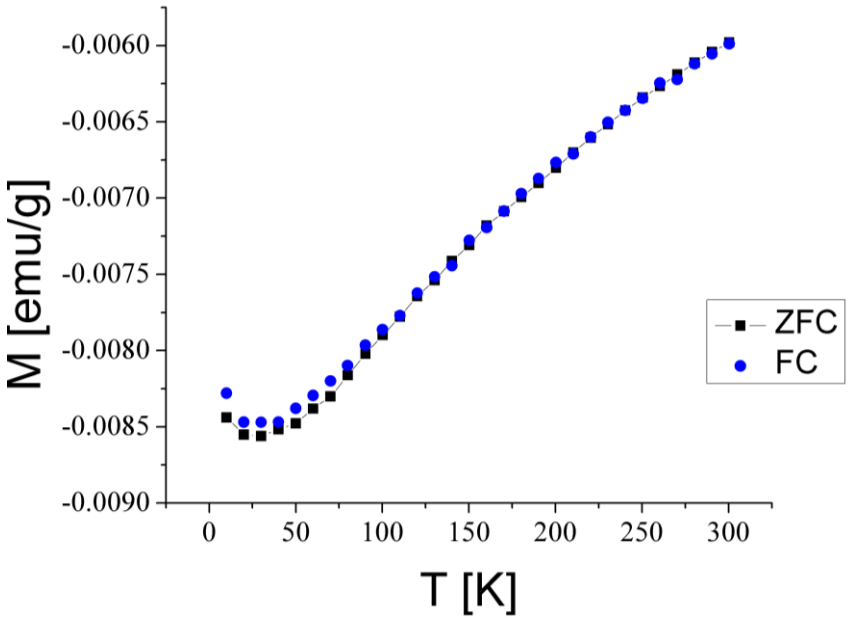


**Figure.12.b.** Magnetization versus temperature plots for fluorinated micro-graphite over 5-300K with an applied field of 500 Oe at FC conditions

The ferromagnetic state with a hysteresis loop observed at 30 K with a coercive field of 200 Oe exists up to a temperature of 125 K. Beyond the blocking temperature of 125 K, the magnetic moments align towards a paramagnetic ordering with no hysteresis loop and zero coercive field. Thus due to increase in thermal energy, a transition from ferromagnetic state to paramagnetic state is observed at 125 K.

The negative slope in the two extremities of plot of magnetization against applied field for hydrogenated micro-graphite **Figure 11 (a)**, as mentioned earlier, indicates a mixture of diamagnetic and magnetic (ferromagnetic and superparamagnetic) signals. Since the diamagnetic signals persist at all temperatures without any change, it is not seen in the FC and ZFC plot. However, the contribution of the non-magnetic portion of the hydrogenated micro-graphite sample is very small, predominantly making the sample

magnetic. Irregularities in the pristine micro-graphite sample, non-uniform fluorination process and inconsistent hydrogenation may have caused the sample to have a portion not induced towards magnetic ordering.

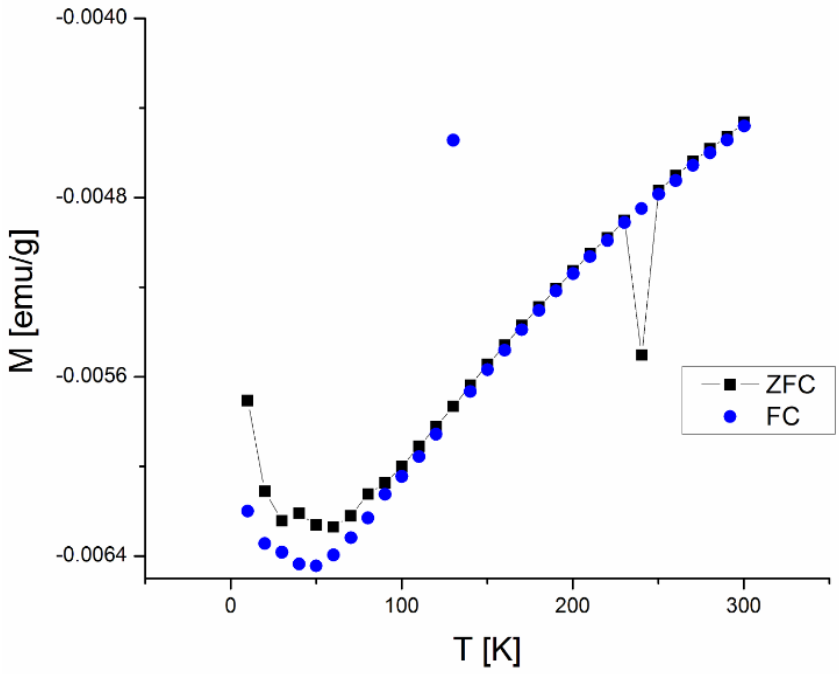


**Figure.12.c.** Magnetization versus temperature plots for pristine micro-graphite over 5-300K with an applied field of 500 Oe at FC conditions

The FC and ZFC plots for fluorinated and pristine micro-graphite samples in **Figures 12 (b) and (c)**, show an overlap of the two curves. This suggests the lack of multiple magnetic states in both the starting material and fluorinated micro-graphite particles over temperatures from 0 K to room temperature. In the case of pristine micro-graphite particles, the magnetization values peak and dip at 140 K and 250 K respectively. Magnetization against the applied magnetic field curves for pristine micro-graphite particles illustrate non-magnetic behavior (**Figure 11 (b)**). Hence, the peak and

dip do not suggest any change in magnetic states and may have originated either from the capsule or from the instrumentation error.

To further investigate the crucial role of hydrogenation and to also verify if the CVD hydrogenation truly induces magnetism in micro-graphite, higher volumes of fluorinated micro-graphite particles were exposed to increased flow rates of hydrogen gas. **Figures 13 (a) and (b)** show the plot of magnetization as a function of applied magnetic field for hydrogenated micro-graphite samples exposed to 0.4 liters/min of hydrogen (double the original flow rate of hydrogen). Originally, SQUID analysis performed on this sample showed diamagnetic behavior. The same hydrogenated micro-graphite sample when divided into 4 parts and separately analyzed using SQUID exhibited magnetic (paramagnetic) ordering in one of the 4 samples, as shown in **Figure 13 (a)**. The remaining 3 samples exhibited non-magnetic (diamagnetic) ordering of moments at 30 K as shown in **Figures 13 (b)**.

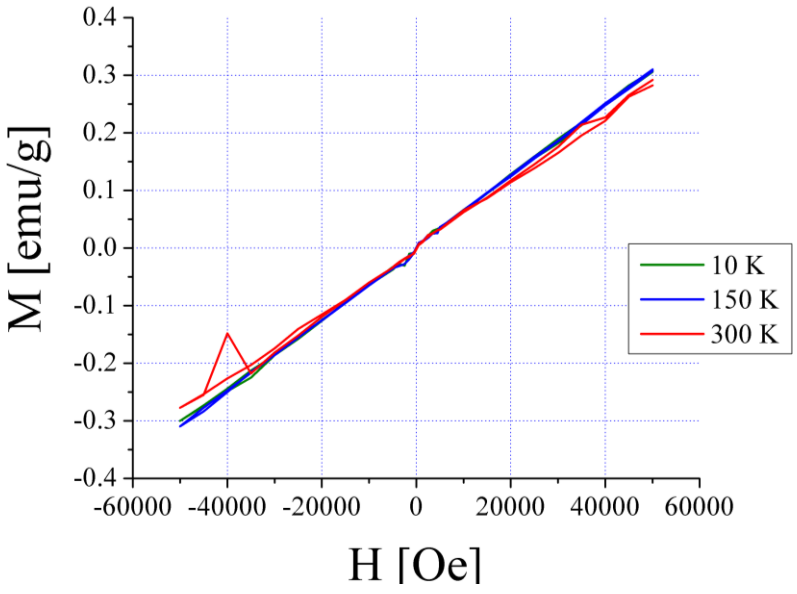


**Figure.13.a.** Magnetization versus applied field plots for hydrogenated micro-graphite showing paramagnetic behavior at 10, 150 and 300K.

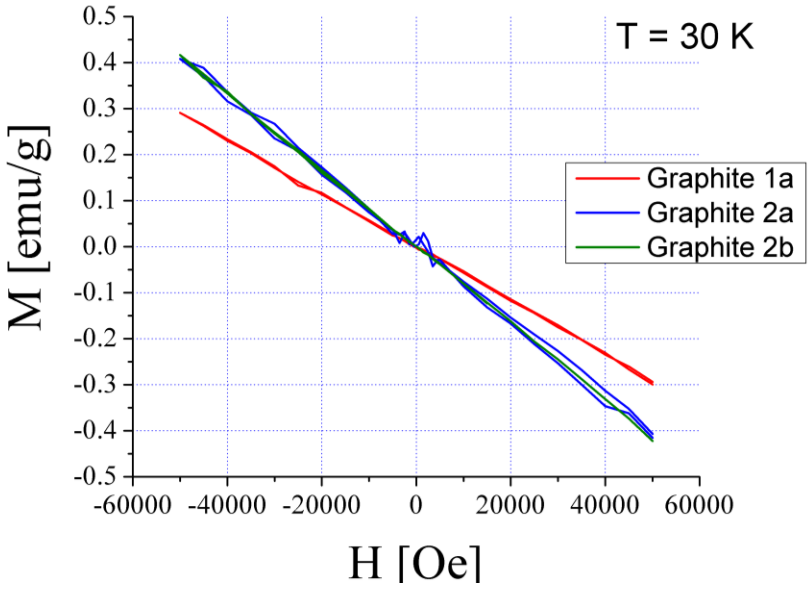


**Figure.13.b.** Magnetization versus applied field plots for 3 hydrogenated samples showing non-magnetic behavior at 30K.

Two important concerns arise from the above plots. Firstly, why does most of the sample volume exhibit non-magnetic behavior? Further, why does paramagnetic ordering arise instead of either superparamagnetic or ferromagnetic ordering as observed earlier? In the CVD processing with increased hydrogen exposure, the sample volume taken in each of the quartz crucibles were much greater (about five fold) than the fluorinated samples processed earlier. Since the crucibles are of small dimensions, with a diameter about 2 cm, this could significantly affect the exposure of defect sites buried away from exposure to hydrogen gas. As shown earlier, lack of hydrogenation of pyrolyzed fluorinated samples exhibit diamagnetic behavior. Hence, most of the sample displays non-magnetic ordering due to non-uniform hydrogenation. The top surface of the sample exposed to hydrogen gas, undergoes hydrogenation and would contribute to the magnetic

signal. This explains why a fraction of the predominantly non-magnetic sample when analyzed displays magnetic ordering.

As discussed earlier, only the upper surface of the sample volume in the quartz crucible was exposed to hydrogen. Hence, the volume of hydrogen gas exposure per unit area of sample was higher in contrast to the prior CVD processing. In order to address the next concern regarding the paramagnetic behavior of hydrogenated micro-graphite particles, the graphite lattice structure and its role in shaping the magnetic ordering will be discussed. **Figure 14** illustrates the crystal lattice structure of graphite. Here the carbon atoms are represented as colored circles with red and blue depicting the two sub-lattices that make up the graphite structure. The Hubbard model, a simple model for interaction of particles within the lattice, also highlights the importance of stacking order of graphite in inducing ferromagnetism. The pristine micro-graphite samples exist as fraction products and such irregularities could have lead to paramagnetic ordering.

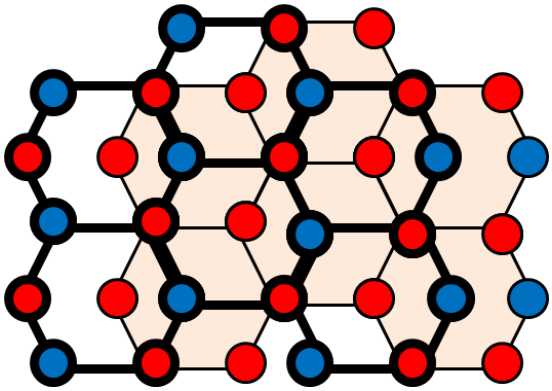

**Figure.14.** Graphite lattice structure

Theoretical calculations involving irradiated graphite using the Hubbard model conclude that an unequal distribution of chemical functionalization between the two sub-

lattices is required for ferromagnetic ordering.(14, 33) Uniform chemical functionalization may lead to magnetic ordering across the two sub-lattices to cancel out each other (due to opposing moment orientations). In the presence of an applied magnetic field these moments will align in a particular direction and behave in an additive fashion. This confers the paramagnetic ordering to the micro-graphite particles as observed in **Figure 13 (a)**.

Although the magnetization verses applied field plots **(Figures 11 (a), 13 (a))** show different magnetic ordering (ferromagnetic, superparamagnetic and paramagnetic), nevertheless demonstrates the possibility of inducing magnetism in graphite by hydrogenation.

## 2.7. Conclusion

The SQUID characterization provides evidence for the magnetization of micro-graphite particles through the CVD hydrogenation protocol. The NEXAFS spectra confirm the hydrogenation of defect sites induced through chemical synthesis process. Confirming to theoretical models, the induction of $sp^3$ defects in micro-graphite established by Raman induced irreversible magnetism. The SQUID measurements for pristine micro-graphite measurements considered alongside trace metal analysis data (ICP-OES) highlight two key findings. Primarily, the magnetization in hydrogenated micro-graphite particles originates inherently from the graphitic structures and not from metallic contaminations. This confirms the origin of graphite magnetism. More importantly, the vital role of hydrogen in inducing graphite magnetism is established.

## Chapter.3. Relaxometry Studies

### 3.1. Nuclear Magnetic Relaxation Dispersion (NMRD)

NMRD profiles are proton-spin relaxivities measured as a function of magnetic field. Nuclear magnetic relaxation dispersion (NMRD) profiles can be of great help in determining the parameters influencing relaxation, and have played an important role in the development of our understanding of proton relaxation rates. In general, the NMRD profile is a plot of the relaxation rate (inverse of either one of the relaxation times T1, T2), R1 or R2 as a function of magnetic field.

#### 3.1.1. Sample Preparation and Instrumentation

Hydrogenated graphite particles in pluronic solution at a concentration of 0.4mg/ml were sonicated for uniform dispersion. This dispersion was then dissolved in 4% gelatin solution in 1:1 volume ratio, yielding a 0.2 mg/ml concentration of hydrogenated micro-graphite particles. A Field cycling NMR relaxometer with capabilities to measure T1 and T2 over the frequency range of 5 to 50 MHz was employed. The relaxation time values were recorded at a temperature of 298 K.

#### 3.1.2. Results and Discussion

Proton relaxation rate measurements of hydrogenated micro-graphite particles at a concentration of 0.2 mg/ml (in 1:1 pluronic and 4% gelatin solution) are shown in **Figures 15 (a) and (b)**. Here **figures (a) and (b)** represent the NMRD plots for spin-

lattice relaxation rate (R1) and spin-spin relaxation rate (R2) values of hydrogenated micro-graphite particles respectively. The R1 relaxation rates for the hydrogenated micro-graphite and control samples (1:1 mixture of pluronic and 4% gelatin) are similar, revealing no further shortening of T1 relaxation times for water protons. In **Figure 15 b** showing the R2 values, the relaxation rates for water protons are significantly higher than the background value of 0.4 $sec^{-1}$ (not shown in figure) and control sample relaxation rates. During R2 measurements, the time difference between the RF excitations at 90° and 180° is referred to as Tau. If the sample under investigation sends out a magnetic signal of its own, as in the case with superparamagnetic materials, R2 measurements differ with Tau values. The R2 measurements were investigated at Tau values of 1, 3 and 5 seconds.

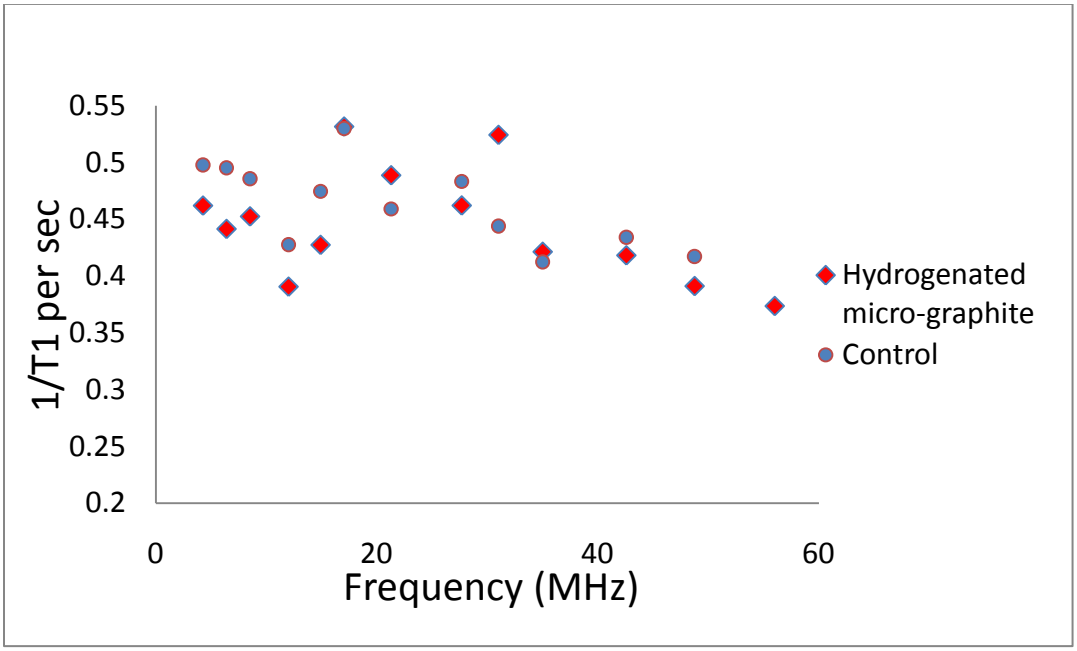


**Figure.15.a.** NMRD plot of R1 relaxation rates observed for 0.4 mg of hydrogenated micro-graphite (in pluronic and 4% gelatin) and control (pluronic and 4% gelatin)

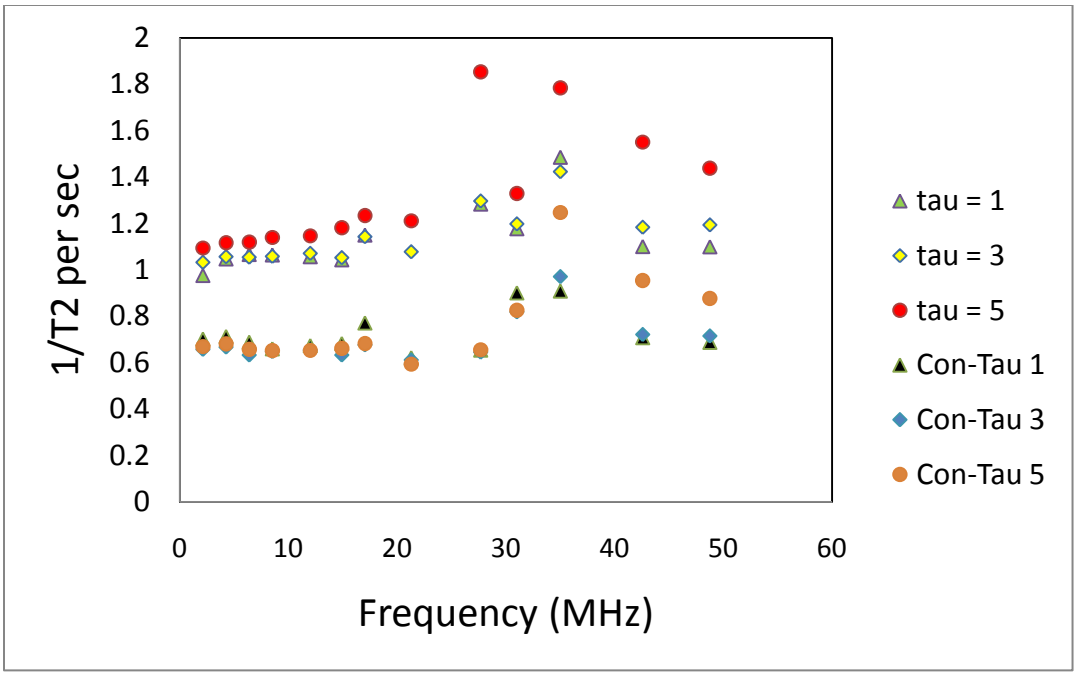


**Figure.15.b.** NMRD plot of R2 relaxation rates observed for 0.4 mg of hydrogenated micro-graphite (in pluronic and 4% gelatin) and control (pluronic and 4% gelatin)

Materials like superparamagnetic iron oxide (SPIO) particles displaying superparamagnetic behavior predominantly shorten T2 values but sometimes also reduce T1 relaxation times.(57) Since these hydrogenated micro-graphite particles exhibit superparamagnetic behavior above 150 K **(Figure 11 (a))**, T2 relaxation times were shortened by the presence of the magnetic particles. At different Tau values, the R1 remains constant for a particular applied magnetic field if the sample does not emit any signal of its own. In case of samples sending out magnetic signals of their own, non-uniform local field alters relaxation rates across tau values. Such local field variability altering R2 values is observed at a tau value of 5 seconds. This could either be due to the irregularities in the distribution of magnetic ordering across the sample or due to the contribution from the pluronic gelatin solution, as seen in the Con-Tau 5 curve. The T2

profiles show a peak at around 30 - 40 MHz. At about 27 MHz, there is a second peak observed (at tau=3) for hydrogenated micro-graphite sample. The origin of this peak could either be due to the sample emitting its own magnetic signal or may be due to irregular distribution of the magnetic ordering across the sample. Nevertheless, this data suggest that the hydrogenated micro-graphite particles shorten R2 values for surrounding water protons, thereby increasing contrast. With more uniformity in distribution of magnetic ordering and stronger magnetic moment, the hydrogenated micro-graphite samples hold the potential to significantly decrease spin-spin relaxation times.

### 3.2. MRI Phantom Imaging

Phantom imaging is the technique in which an object with a magnetic resonance signal is imaged in a MRI system. The phantoms are inanimate objects and are employed as standards to evaluate the performance of MRI systems. Phantoms standards are replacements for human standard samples as they are easier to produce and transport.

Phantom imaging is widely performed to standardize MRI systems and to determine and compare the performance of contrast agents. Here, the contrast agents are dissolved or dispersed in a signal bearing substance. Such substances enable the measurement of spin-lattice (T1) and spin-spin (T2) relaxation times. Water, agarose gels, silicone and polyacrylamide gels are commonly used signal bearing substances. The contrast agent materials in solution or gels containing of signal bearing substances are referred to as phantoms as well. On imaging the contrast enhancement in each of the phantoms, a qualitative comparison between the contrast agents can be presented.

The phantom imaging can be operated through two modalities; T1 Weighted and T2 Weighted imaging. All materials, including tissue samples posses both T1 and T2 relaxation. In the case of Weighted T1 imaging, most of contrast observed (either between tissue samples or phantoms) is primarily due to the differences between the spin-lattice relaxation time (T1) values. Similarly, the contrast observed in Weighted T2 imaging modality is mainly due to differences in the spin-spin relaxation times (T2). For instance, the commercially available gadolinium based contrast agent Magnevist has a predominant T1 reduction effect compared to T2. Hence Magnevist is clinically used under weighted T1 modality as it produces better contrast.

By altering parameters like repetition time (TR) and echo delay time (TE) in the MRI system, weighted T1 and T2 imaging can be performed. A T1 contrast image is obtained at low TR and TE values and in contrast, by altering the parameters to high TR and TE values weighted T2 images are obtained. For human tissue imaging, weighted T1 imaging is carried out with TR values typically below 500ms and TE values lower than 30ms. In the case of weighted T2 imaging, TR above 2000ms and TE values typically above 100ms are used.

### 3.2.1. Sample Preparation and Methodology

The micro-graphite samples were prepared by the NMRD sample preparation protocol mentioned earlier. Briefly, the hydrogenated micro-graphite particles were dispersed in 0.4mg/ml pluronic solution by sonication. Further, this dispersion was dissolved at 1:1 volume ratio in 4% gelatin solution. A final concentration of 0.2 mg/ml

of hydrogenated micro-graphite particles was obtained. As a positive control, 0.1mM of commercially used contrast agent Magnevist diluted in 4% gelatin at 1:1 volume ratio was used. Pluronic (04.mg/ml) and 4% gelatin solutions taken at 1:1 volume ratio was used as control. For the phantom imaging, 0.5cc of the control and hydrogenated micro-graphite solutions were taken in 5mm NMR tubes.

For weighted T1 imaging, the TE and TR values were set at 5ms and 17ms respectively. The TE and TR values for weighted T2 imaging were set at 60ms and 3600ms respectively. Three dimensional phantom imaging was carried out by recording the weighted images as slices at varying heights with a slice thickness of 2mm.

### 3.2.2. Results and Discussion

Three dimensional weighted T1 and T2 imaging results of control, hydrogenated micro-graphite and Magnevist phantoms are shown in **Figures 16 and 17** respectively. In both the figures, phantom image slices labeled **(a)** indicates the gelatin in pluronic (1:1 volume ratio) solution. Image slices **(b)** represent hydrogenated graphite particles dispersed in the control solution and the image slices for the commercial contrast agent Magnevist is indicated as **(c)**. Phantom image slices in each horizontal row were recorded at fixed heights in the NMR tube.

The weighted T1 phantom images for Magnevist shows better contrast in comparison to the control and hydrogenated micro-graphite particles, as indicated in **Figure 16**. Magnevist is a gadolinium based paramagnetic T1 contrast agent. The di-N-methylglucamine salt of gadopentetate in Magnevist produces a contrast enhancing

effect. Although primarily used as T1 contrast agent, Magnevist also displays T2 contrast enhancement. For clinical use, 0.1-0.3mM/kg of Magnevist is administered in patients. For a Magnevist concentration of 0.2mM used here, the high contrast observed is expected.

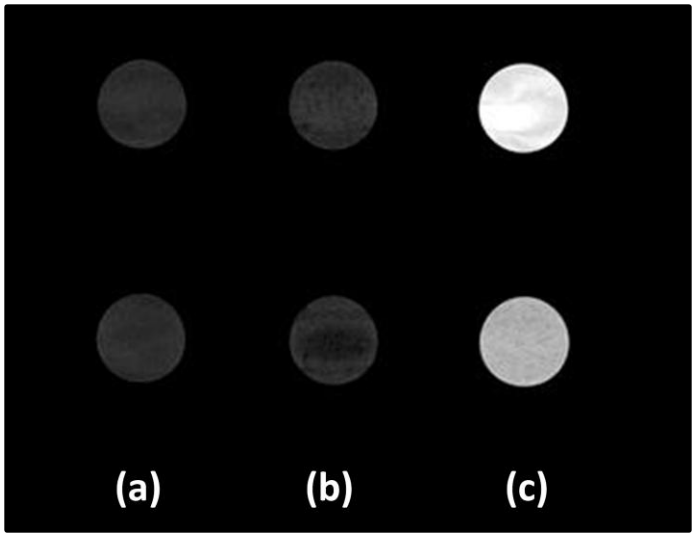


**Figure.16.** Weighted T1 Phantom Imaging of (a) pluronic + gelatin (control), (b) 0.4 mg of hydrogenated micro-graphite in pluronic + 4% gelatin and (c) 0.2 mM of Magnevist in pluronic + 4% gelatin at 1.5 T magnetic field.

The weighted T2 phantom images shown in **Figure 17** indicate increase in contrast for hydrogenated micro-graphite particles and Magnevist compared to the contrast observed in the control phantom image slices. A subtle difference is observed between the hydrogenated micro-graphite and Magnevist phantom image slices, with slight increase in contrast for commercial contrast agent. Magnevist also exhibits T2

shortening effect as mentioned earlier and the high contrast observed in the phantom image slices is as expected. An interesting observation here is the high contrast observed for hydrogenated micro-graphite by weighted T2 MRI which was absent for weighted T1 MRI. SQUID evidence for the hydrogenated micro-graphite indicates the particles exhibit superparamagnetism at room temperature.

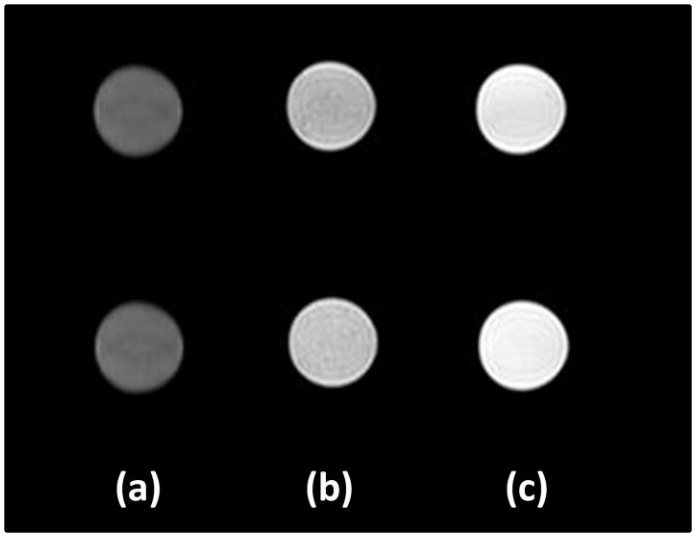


**Figure.17.** Weighted T2 Phantom Imaging of (a) pluronic + gelatin (control), (b) 0.4 mg of hydrogenated micro-graphite in pluronic + 4% gelatin and (c) 0.2 mM of Magnevist in pluronic + 4% gelatin at 1.5 T magnetic field.

Superparamagnetic materials possess magnetization of their own which are evident only in the presence of an applied magnetic field. As a consequence, superparamagnetic materials produce a magnetic field of their own and produce variations in the local magnetic field. This variation enhances T2 relaxation rates and hence the ratio of T2 to T1 for superparamagnetic materials is high. For instance, in the

case of superparamagnetic contrast agents like Combidex and Sinerem the ratio of T2 to T1 is high and show high contrasts at weighted T2 imaging. Hence high contrasts are as expected for the hydrogenated micro-graphite particles exhibiting superparamagnetism. Despite the SQUID data suggesting the presence of a small proportion of hydrogenated micro-graphite particles being non-magnetic, high contrast was observed. Optimizing the sample processing protocol to induce complete magnetism in micro-graphite particles holds the key to further increasing the T2 contrast observed here. The MRI phantom imaging study shows promise for the application of hydrogenated micro-graphite particles as T2 contrast agents.

### 3.3. Conclusion

Since the hydrogenated micro-graphite samples exhibit superparamagnetic behavior at room temperatures, the samples produce magnetic fields in response to applied magnetic fields. As a consequence, superparamagnetic materials are capable of shortening T2 relaxation times and produce contrast in MRI. In agreement, the NMRD profiles show shortening of T2 relaxation times. Correspondingly, the MRI phantom images indicated significantly better contrast enhancement at weighted T2 MR imaging as expected. The relaxometry data strongly suggests the potential application of magnetic micro-graphite particles as superparamagnetic contrast agents for blood pool imaging. Future studies with better yields of micro-graphite must be performed to fully realize the potential of these micro-graphite particles for MRI.

## Chapter 4: Biocompatibility of Micro-Graphite Particles

### 4.1. Effect of Micro-Graphite on In-Vitro Cell Viability

Establishing biocompatibility and safety are the foremost important steps towards developing magnetic graphite for biomedical applications such as MRI CAs. Most commonly used Gd-based T1 CAs or Fe-based T2 CAs use chelating ligands or biocompatible coatings to sequester the toxicity of naked gadolinium (Gd) and iron (Fe). However, these toxicity-sequestering strategies may not be adequate as recent reports associate clinical Gd-based agents CAs with acute renal failure.(87) Graphite is generally known to be biocompatible and has found uses among many others in dental and skeletal implants as well as coatings on heart valves.(68, 69, 71) Graphite has been popularly used as a coating material to improve the biocompatibility and integrity of metal nanoparticles for drug delivery and imaging applications.(74, 88)

For applications like MRI contrast agents for blood pool imaging, short retention times in the order of 2 to 24 hours in body are sufficient. In order to compare the toxicity of metal atoms against micro-graphite particles, a short term cell viability assay was performed. Iron, gadolinium and manganese were the metals chosen for the viability studies as they find popular applications in contrast agents for medical imaging.

Nascent metals are highly toxic and are always coated with or encapsulated in a biocompatible material. Although such processing reduces the toxicity of such metal ions to a certain extent, the degradation of encapsulations in the body leading to free metal ions remain a cause of concern. This study weighs the toxicity of such metal ions against micro-graphite particles.

## 4.2. Materials and Methods

### Calcein AM Viability Assay:

Calcein viability assay (purchased from Molecular probes, Invitrogen) was performed on J774.a1 cells. The kit consists of Calcein AM (Aceto Methoxy derivative of Calcein), a cell permeable non fluorescent dye. In the case of live cells, the intracellular esterases actively cleave the acetomethoxy group from calcein. This converts the dye to its fluorescent configuration with intense green emission.(89, 90) Dead cells do not possess active esterase activity and hence do not cleave Calcein AM. Thus only the live cells are labeled.

### Cell line:

J774.a1 (henceforth referred to as J774 cells) murine macrophages purchased from ATCC were used for the viability studies. Macrophages are an important component of the defense mechanism in the immune system. These cells act on foreign materials and actively try to digest them in a process known as phagocytosis. The average diameter of J774 macrophages are about 22 μm, similar to that of the micro-graphite particles analyzed here. Further, J774 cells display active phagocytic activity, making them the ideal candidate for studying in vitro toxicity effects of the micro-graphite particles.(91, 92)

### Groups:

In this study, the effect of 4 different materials on the viability of J774 cells was investigated. The materials were micro-graphite, manganese, gadolinium and iron

particles. The micro-graphite samples were dispersed in DSP-PEG. Chloride salts of manganese, gadolinium and iron were dissolved in pH=7.4 (physiological pH) adjusted water. Cells treated with extra media equivalent to the treatment volume were treated as controls for the viability assay.

**Control:**

Macrophage cells without the treatment of any of the experimental groups were the controls at each time point. The sample volume of treatment samples were 20 µl and to the control cells, additional media of 20 µl were added to control for volume across wells. The fluorescence intensity values for the control groups at each time point were used to normalize the data for the experimental groups.

**Table.2.** Experimental Treatment Groups for the viability assay

| **Experimental Groups** |
|---|
| Micro-graphite |
| Manganese |
| Gadolinium |
| Iron |

**Treatment concentration:**

The treatment concentrations studied were 1, 10, 20, 40 and 80ng/ml (prepared by serial dilutions). These values were specifically chosen to understand the toxicity of graphite at low dosages, required for medical imaging. Experimental investigations of

iron based blood pool agents like Ferumcarbotran and Ferumoxtran-10 indicated an iron content of about 10-50pg/cell. With approximately 1000 cells per well, treatment volumes were chosen around 50ng/ml (50pg/cell X 1000 cells = 50ng). All treatment solutions were pH adjusted (pH=7.4) and sterilized by UV radiation before adding it to the wells.

**Time points:**

The plates were analyzed at 6, 12 and 24 hours from the time of treatment to study the effect of the treatment materials on macrophage viability. Individual plates were maintained for each time point. The experiment was carried out in triplicates.

**Methods:**

J774 macrophage cells were cultured in high glucose Dulbecco's Modified Eagle's Medium (DMEM) supplemented with 7% fetal bovine serum and 1% antibiotics (penicillin and streptomycin). Trypsin treatment degrades cell surface receptors on J774 cell, altering their phagocytic activity. Thus cell scrapping was adopted for passaging the macrophages. To prevent any background signal from the media, colorless DMEM (without the indicator) was used. The macrophages were seeded at a density of $1X10^4$ cells per well in 96 well plates (one plate per time point) and incubated overnight to ensure the attachment of cells to the bottom of the plate. Treatments of graphite, manganese, gadolinium and iron were given at the above mentioned concentrations the

next day, referred to as the zero time point. Cells treated with extra media equivalent to the volume of treatment solutions were used as controls for the viability studies.

Appropriate dye concentration specific to the J774 macrophage cell line was adopted from the kit manufacturer's protocol. Solutions of 2µM of Calcein AM were prepared freshly for each time point by diluting 5µL of 4mM calcein AM solution in 10mL PBS.

Media was removed and the wells were washed twice with 100 µL of PBS at 6hr, 12 hr and 24 hr time points. Next, 100 µL of the Calcein AM dye was added to the wells and incubated for 30 minutes. During the incubation period, precaution was taken to prevent photobleaching of the dye by wrapping the plates with aluminum foil. Dye preparation and treatments were carried out under minimal yellow light conditions. After incubation, the plates were analyzed using a fluorescent plate reader. The plates were excited at 485±20 nm and the fluorescent emissions were recorded using a 530±20 nm filter.

**Statistics:**

Significance of differences between means was calculated using first by One way analysis of variance (ANOVA) for each time point and across time points using Multi way analysis of variance (MANOVA) using the SPSS (version 17.0) software package. Tukey's honestly significant difference post hoc test was employed to identify any specific trends in the subgroup of samples. p-values below 0.05 were considered significant.

### 4.3. Results and Discussion

Fluorescence intensities were measured at 530 nm and plotted for all treatment samples at different treatment concentrations and time points. The relative viability of the cells treated with different materials is directly proportional to the observed fluorescent intensities. **Figures 18 (a-c)** show the relative viability of J774 macrophages treated with increasing concentrations of graphite particles, manganese, iron and gadolinium at the end of 6, 12 and 24 hours, respectively. The data presented in these figures not normalized with respect to the fluorescent intensity values obtained for cells treated with extra media (control) for specific time points. Error bars indicate standard error of mean.

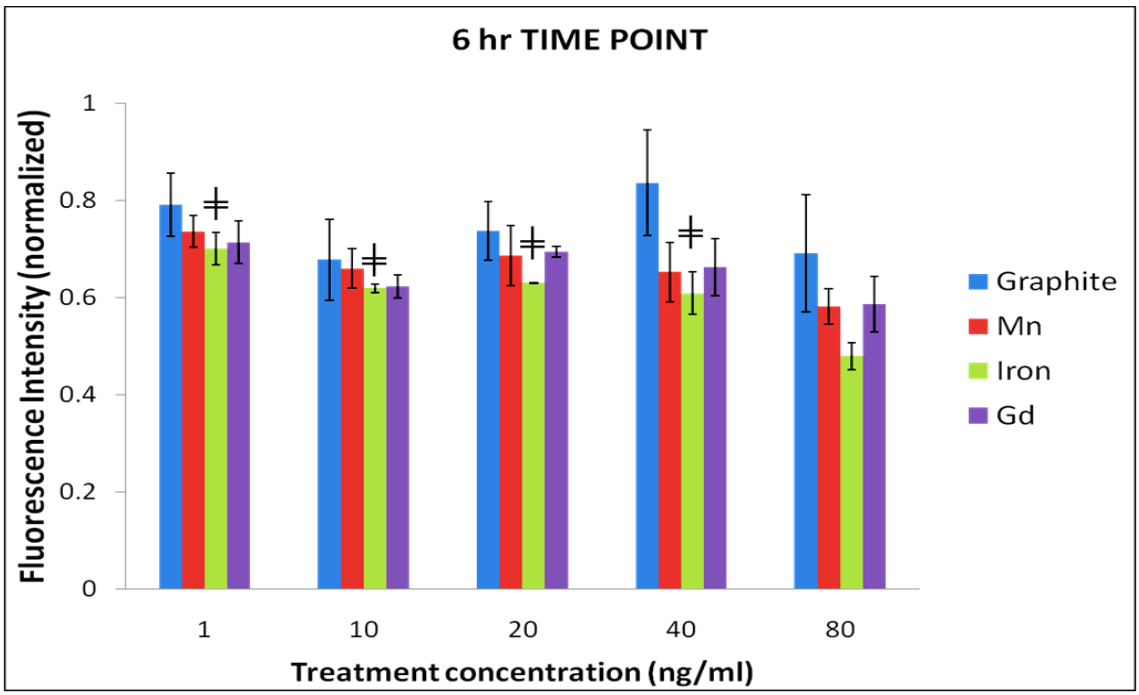


**Figure.18.a.** Viability of J774 cells treated with increasing concentrations of graphite, iron, manganese, and gadolinium at the end of 6 hours are represented as normalized fluorescent intensity values. (Fluorescent intensities normalized with respect to

fluorescent intensity control group treated with extra media well fluorescence intensities) (╪: p<0.05w.r.t. 80ng/ml Iron treatment)

At the end of 6 hours, as shown in **Figure 18 (a)**, the viability of the J774 cells is reduced significantly for 80ng/ml treatment of iron compared to the viability for iron treatment concentrations of 1, 10, 20 and 40ng/ml. The fluorescent intensity values are normalized to the control group fluorescence of 5330±522 nm at 6 hours. The viability of macrophages treated with iron at 80ng/ml was significantly lower than the graphite and manganese treatment at the same concentration. With the exception of J774 cells treated with 40ng/ml of graphite, all other treatment groups show significant reduction in viabilities.

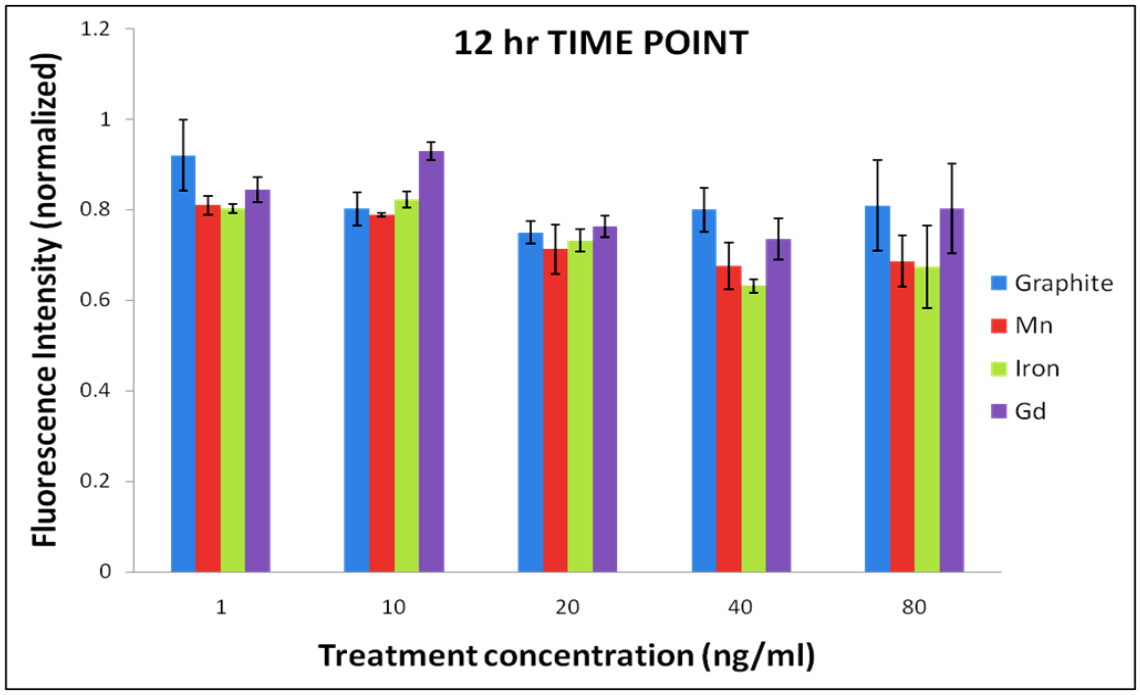


**Figure.18.b.** Viability of J774 cells treated with increasing concentrations of graphite, iron, manganese, and gadolinium at the end of 12 hours represented as normalized

fluorescent intensity values. (Fluorescent intensities normalized with respect to fluorescent intensity control group treated with extra media well fluorescence intensities)

**Figure 18 (b)** shows the viability of J774 cells at the end of 12 hours. A significant reduction in J774 cell viability is observed at 40ng/ml treatment of iron as against all lower treatment concentrations of iron. Compared to the viability of the control group, significant decrease in viability is observed for 40ng/ml and 80ng/ml treatments of manganese and iron.

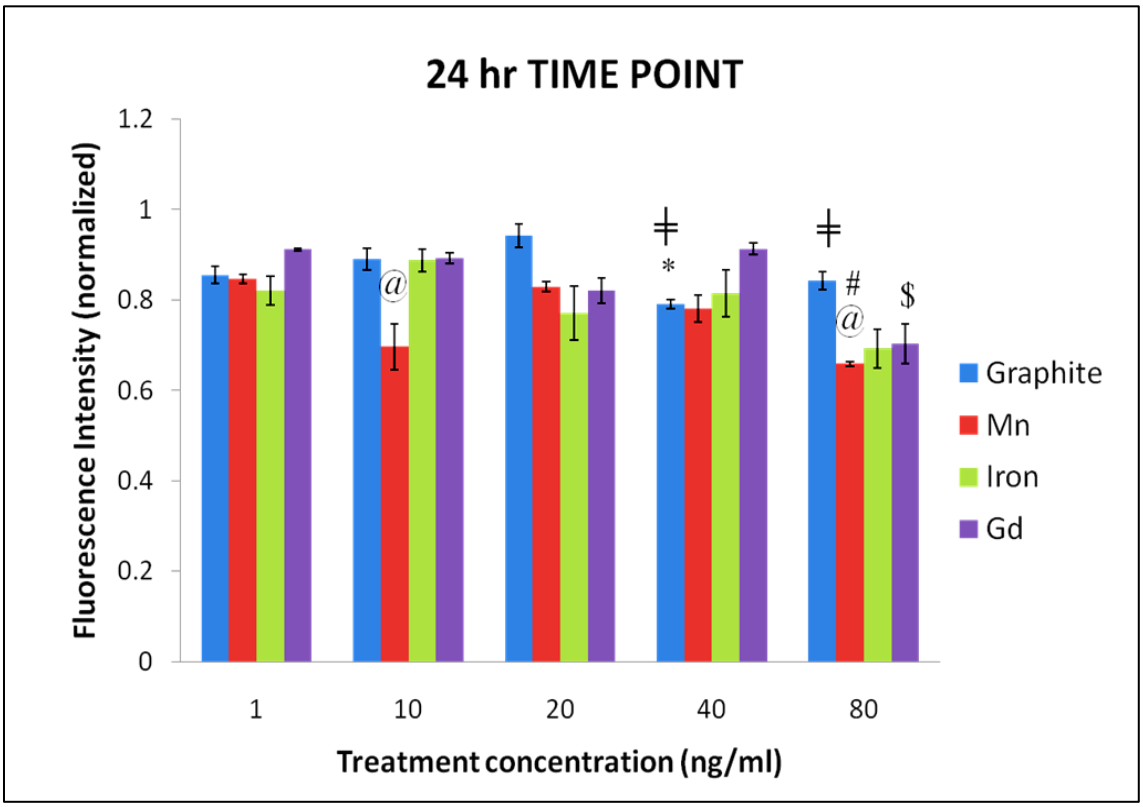


**Figure.18.c.** Viability of J774 cells treated with increasing concentrations of graphite, iron, manganese, and gadolinium at the end of 24 hours represented as normalized fluorescent intensity values. (Fluorescent intensities normalized with respect to

fluorescent intensity control group treated with extra media well fluorescence intensities) (*: $p<0.05$w.r.t. 10ng/ml graphite treatment, ╪: $p<0.05$w.r.t. 20ng/ml graphite treatment, @: $p<0.05$w.r.t. 1ng/ml manganese treatment, #: $p<0.05$w.r.t. 20ng/ml manganese treatment, $: $p<0.05$ w.r.t. all other gadolinium treatments)

Significant differences were observed at certain concentrations where the J774 cell viabilities for higher treatment concentrations were higher than at lower concentrations. For instance, manganese treatment of 20ng/ml has higher cellular viability than at 10ng/ml as shown in **Figure 18 (c)**. One aspect to noted here is the large error bar value for the 10ng/ml treatment, nevertheless significant differences were observed. A similar scenario is observed between 40ng/ml and 80ng/ml treatments of graphite.

For the 6 hour time point, except the 40ng/ml treatment group of graphite, significant reduction in viabilities was observed. This might be due to the fact that the standard error of mean is high in this case, as indicated in **Figure 18 (a)**. Although the viabilities were expected to reduce with increase in treatment concentration, no such general trend was observed. In the case of the 12 hour time point, shown in **Figure 18 (b)** no general pattern in the viability values was observed, similar to the 6 hour time point data. Significant differences were observed for various concentrations of all groups at the 24 hour time point, as shown in **Figure 18 (c)**. Here, the J774 cell viabilities for higher treatment concentrations were higher in comparison to lower treatment concentration. Such differences remain inconclusive. In comparison with the viability of control cells, significant decrease in viability across all groups at all concentrations is observed.

To better compare the change in viability between the lowest and the highest treatment concentration across time points, the normalized data with respective to the control fluorescent intensity values specific to the time points were plotted as shown in **Figure 19**.

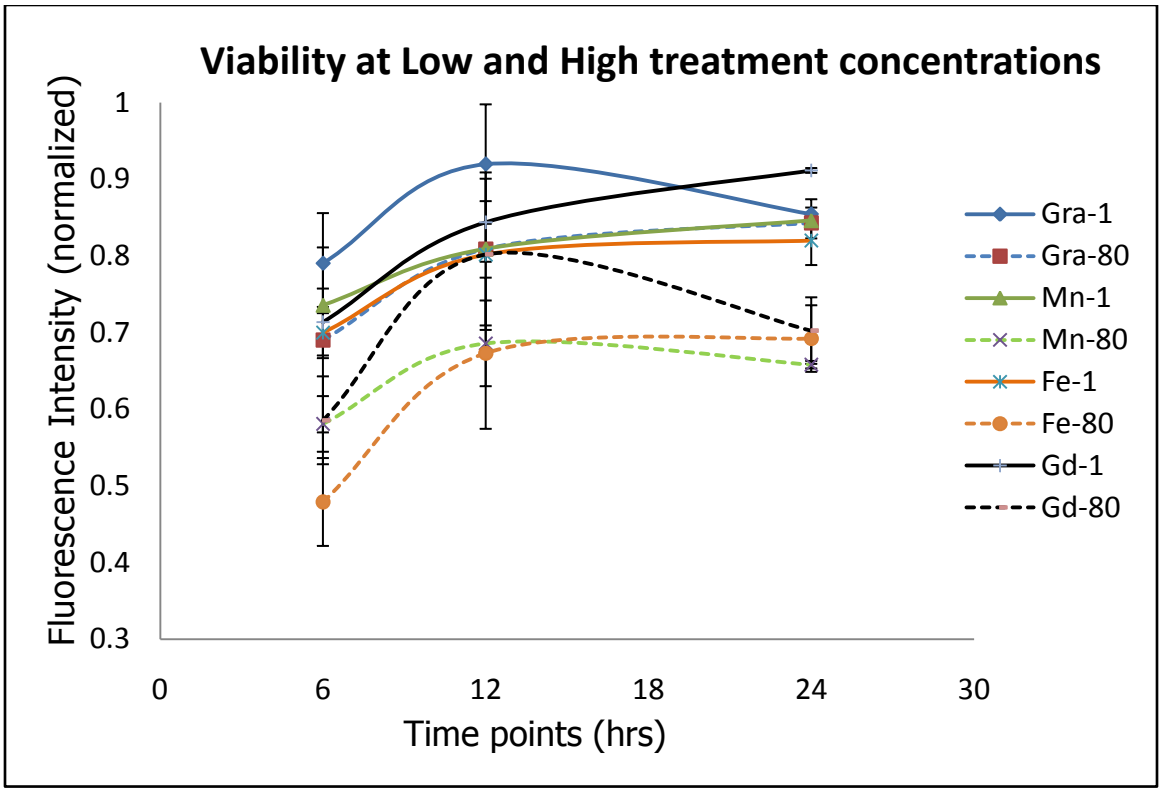


**Figure.19.** Viability of J774 cells at lowest and highest treatment concentrations of graphite, iron, manganese, and gadolinium represented as normalized fluorescent intensities across the study duration. (Fluorescent intensities normalized with respect to fluorescent intensity control group treated with extra media well fluorescence intensities)

The continuous lines in the plot represent the lowest treatment concentrations of 1ng/ml and the dotted lines represent the highest treatment concentrations of 80ng/ml. An

interesting trend is observed across all treatment groups for all treatment concentrations. An upward curve suggesting increase in cell viability is observed between 6 and 12 hour time points for all treatment groups, which are significant for both treatments of iron and gadolinium.

Although significant differences were not observed for graphite and manganese, a trend seems to be emerging. The positive trend can be attributed to two reasons. First, an increase in the cell population leads to increase in the fluorescence values that increase observed viability. The initial seeding rate of cells per well was estimated keeping in mind that the cells would not reach confluency till the end of the study. As the 12 hour time point is close to the 17 hour doubling time, an increase in cell count is expected. The short duration of the 6 hour and 12 hour time point may not be long enough to observe any toxicity conferred by the treatment samples. This might be yet another reason that a relative increase in J774 cell viability is observed. If the duration of 24 hours is insufficient to elicit a cytotoxic response by the treatment samples in J774 cells, an increase in cell viability would have been observed between time points 12 and 24 hours. Interestingly, a trend of a relative decrease in cellular viability is observed for most groups with the exception of 1ng/ml treatment of gadolinium. Although these differences are not significant, they indicate that cytotoxic effects due to the treatments cause a decrease in J774 cell viability.

### 4.4. Conclusion

No clear trend relating the treatment concentrations and macrophage viability was observed at the three time points. As evident from **Figure 19**, treatment of J774 cells with

80ng/ml of graphite produces the least toxic effect compared to 80ng/ml of iron, manganese and gadolinium treatments at 24 hour time point. This suggests that these metals decrease the viability of murine macrophages significantly more than the reduction observed in graphite. Thus micro-graphite appears to be less toxic than iron, manganese and gadolinium at the highest treatment concentration at the 24 hour time point. However, further in vitro and in vivo studies are necessary to corroborate this preliminary conclusion.

## Chapter 5: Conclusion and Future Directions

### 5.1. General Discussion

The micro-graphite particles have been magnetized following the CVD hydrogenation process. Fluorination is one of the key steps in the hydrogenation protocol, creating $sp^3$ defects in the form of carbon-fluorine bonds. Pyrolysis at 900 K following fluorination, removes the fluorine atoms inducing point defects. In the above two cases, the micro-graphite particles have either $sp^3$ defects or missing carbon atoms. As discussed in Chapter 1, such defects have been theoretically shown to be the basis for graphite magnetism. SQUID analysis presented under the magnetic characterization chapter indicated otherwise. Magnetic ordering in micro-graphite particles were observed only in the hydrogenated samples. All the SQUID data including the pristine micro-graphite measurements combined with the metallic impurity measurements (Chapter 2) highlight two important results. First, the magnetic signal observed in hydrogenated micro-graphite particles is inherently from the graphite particles and not from metallic impurities (either from sample handling or processing apparatus). This establishes the evidence for magnetism in graphite and demonstrates the possibility of organic magnetism. Secondly, hydrogen plays a vital role in inducing magnetism in graphite structures.

Raman spectra indicated an increasing loss in $sp^2$ nature of the micro-graphite particles at every stage of the processing leading to hydrogenation. Additionally, the NEXAFS data provided characteristic evidence for C-H bond formation validating the success of the CVD hydrogenation process. Few of the carbon double bonds were destroyed by fluorination and some carbon atoms are lost during pyrolysis. The hydrogen

bonding at these sites ensures carbon sigma bond stability. This alteration in the electron distribution creates a non-zero net magnetic dipole, conferring a magnetic behavior to micro-graphite. Thus, the fundamental questions regarding the origin of magnetism and the role of hydrogen are addressed.

The motivation for developing magnetic micro-graphite particles was to employ them as CAs for MRI blood pool imaging. Relaxometry studies for hydrogenated micro-graphite particles using the NMRD technique help evaluate their performance as potential contrast enhancing materials was evaluated by analyzing the reduction in T1 and T2 values. Although micro-graphite particles showed small reductions in T1 relaxation times, more significant shortening of in T2 relaxation times were observed. MRI phantom imaging was performed to visualize the T2 time shortening and evaluate its ability to enhance contrast. In comparison to the T1 weighted images, hydrogenated micro-graphite particles displayed increased contrast. The increase in contrast appeared to be almost equivalent to the contrast enhancement observed with a commercially available contrast agent. Upon optimization of the processing thereby further increasing the magnetization values, higher contrast can be achieved from hydrogenated micro-graphite particles.

Evaluating the toxicity of hydrogenated micro-graphite particles is critical to develop them into potential contrast agents. Calcein AM based cell viability studies were performed for varying concentrations of these graphite particles along with metals that commonly used in contrast agents. The J774 macrophages were challenged with increasing concentrations over a 24 hour time period. No clear trend establishing increasing toxicity at higher concentrations was observed. Interestingly, the viability of macrophages treated with these graphite particles was higher compared to other metals at

the 24 hour time point for the highest treatment concentration. Performing longer duration studies could help understand the biocompatibility of graphite in relation to these metals. Graphite has been shown to be biocompatible with in vitro and in vivo studies mentioned earlier. Additional proof emphasizing its in vitro and in vivo biocompatibility relative to currently used contrast agents could make the use of graphite based contrast agents more advantageous in terms of large dosages and repeated MRI scans.

## 5.2. Conclusions

Achieving organic magnetism has not ceased to interest researchers involved in both basic sciences and high-tech applications. Theoretical models for various carbon based structures suggest the possibility of inducing magnetism through different approaches. Currently very few theoretical mechanisms to induce magnetism in carbon structures have been validated with experimental evidence. In this thesis, one such theoretical mechanism of inducing magnetism in graphite by producing dangling hydrogen bonds has been presented.

Most published work involving graphite magnetism has used highly oriented pyrolytic graphite (HOPG) samples as the starting material. Recently, investigations on these HOPG samples revealed the presence of magnetic impurities casting doubts on the very existence of graphite magnetism. In the work presented here, extreme caution has been exercised starting from the choice of graphite material, impurities characterization up to studies assessing its magnetic behavior. Analytical grade graphite high purity

micro-graphite particles have been used for inducing magnetism here. Extensive magnetic characterization of micro-graphite particles performed at each processing stage including sample handling eliminates the possibility of magnetic impurities contributing towards the magnetic signal observed from SQUID analyses.

The magnetization values observed for hydrogenated micro-graphite particles and the NEXAFS spectrum indicating the presence of hydrogen bonds establishes the success of the novel CVD hydrogenation process developed here. At higher hydrogenation levels, paramagnetic behavior in micro-graphite particles was seen instead of previously observed superparamagnetic behavior. Repeatability studies across three additional runs confirmed the presence of paramagnetic behavior. This has provided interesting insights into the role of hydrogen and the tunable behavior of magnetism in graphite. NMRD profiles indicated shortening of T2 values, corresponding to its superparamagnetic behavior. MRI phantoms comprising of these magnetic graphite particles were visualized under weighted T1 and T2 imaging and contrast enhancement was observed in weighted T2 MR imaging as expected.

Biocompatibility of graphite has been observed in coatings for prosthetic implants, cell in-growth and cell proliferation studies. Graphite particles are promising candidates for contrast enhancing materials due to their magnetic behavior and biocompatibility. The large size of graphite particles combined with its albumin binding properties make them ideal suited for blood pool agent applications. The biocompatibility of graphite alongside commonly used metals in contrast agents was assessed. The results displayed no general trend in variation of viability with treatment concentration. At the 24 hour time point, graphite displayed significantly higher biocompatibility in

comparison to the other metals at the highest treatment concentration. The results seem inconclusive regarding the pattern of toxicity as well as long term effects of graphite and metals to cells. Further studies with longer time points would help understand the trends in viabilities. The safety of graphite is well published and with additional data, compatibility of graphite can be established with confidence.

Thus, some of the major issues around the field of graphite magnetism have been addressed here. Magnetism in graphite has been shown to be independent of metallic impurities, multiple types of magnetic behavior has been induced in graphite providing stronger evidence towards carbon magnetism and macroscopic amounts of graphite with high magnetization values have been reported here.

### 5.3. Future Direction

Paramagnetism and superparamagnetism has been achieved in micro-graphite particles, providing strong evidence for carbon based magnetism. Fluorination and hydrogenation processes were carried out under controlled parameters. In order to address the variability in the production of magnetic graphite, the overall processing method must be further optimized and standardized to achieve repeatability. On a separate note, easier alternatives to fluorination for inducing defects must be explored. This would not only improve repeatability but also simplify the scale up process for large scale productions.

High magnetization levels can be achieved by the optimized processing and additional characterization studies to determine its contrast enhancing ability must be

performed. Relaxometry studies must be performed on magnetic graphite obtained from the optimized protocol. Further, it would be interesting to determine their relaxivity profiles at higher magnetic fields as current MRI scanners are designed with increasing fields. MRI studies with the magnetic micro-graphite particles injected in small animals must be performed small animals to better evaluate its performance as a contrast agent along with the in vivo biocompatibility studies. In order to develop graphite particles towards clinical contrast agents, rigorous studies assessing the short term and long term toxicity must be carried out. In addition to these studies, the graphite clearance mechanism in humans must be identified. Finally, the efficacy of graphite based contrast agents must be compared against the current gold standards clinically used. On performing these studies, the clinical application of graphite based contrast agents for blood pool imaging could be achieved, which have the potential to revolutionize MRI based diagnostics.

Bibliography


1. Makarova T & Parada F (2006) *Carbon-based magnetism: an overview of the magnetism of metal free carbon-based compounds and materials* (Elsevier Science).

2. Ugeda MM, Brihuega I, Guinea F, & Gómez-Rodríguez JM (Missing Atom as a Source of Carbon Magnetism. *Physical Review Letters* 104(9):096804.

3. Iijima S (1991) Helical microtubules of graphitic carbon. *Nature* 354(6348):56-58.

4. Dresselhaus M, Dresselhaus G, Eklund P, & Jones D (1996) *Science of fullerenes and carbon nanotubes* (Academic Press San Diego).

5. Rode A, Gamaly E, & Luther-Davies B (2000) Formation of cluster-assembled carbon nano-foam by high-repetition-rate laser ablation. *Applied Physics A: Materials Science & Processing* 70(2):135-144.

6. Harris P, Hernández E, & Yakobson B (2004) Carbon nanotubes and related structures: new materials for the twenty-first century. *American Journal of Physics* 72:415.

7. Mills B (2007) Graphite structure. (Flexbook).

8. Makarova T (2004) Magnetic properties of carbon structures. *Semiconductors* 38(6):615-638.

9. Mombrú A, *et al.* (2005) Multilevel ferromagnetic behavior of room-temperature bulk magnetic graphite. *Physical Review B* 71(10):100404.

10. Esquinazi P (2002) Ferromagnetism in oriented graphite samples. *Phys. Rev. B* 66:024429.

11. Esquinazi P (2003) Induced magnetic ordering by proton irradiation in graphite. *Phys. Rev. Lett.* 91:227201.

12. Lehtinen PO (2004) Irradiation-induced magnetism in graphite: A density functional study. *Phys. Rev. Lett.* 93:187202.

13. Yazyev OV (2008) Magnetism in disordered graphene and irradiated graphite. *Phys. Rev. Lett.* 101:37203.

14. Yazyev OV & Helm L (2007) Defect-induced magnetism in graphene. *Phys. Rev. B* 75:125408.

15. Park N (2003) Magnetism in all-carbon nanostructures with negative Gaussian curvature. *Phys. Rev. Lett.* 91:237204.

16. Cervenka J, Katsnelson MI, & Flipse CFJ (2009) Room-temperature ferromagnetism in graphite driven by two-dimensional networks of point defects. *Nat Phys* 5(11):840-844.

17. Khveshchenko D (2001) Ghost excitonic insulator transition in layered graphite. *Physical Review Letters* 87(24):246802.

18. Khveshchenko D (2001) Magnetic-field-induced insulating behavior in highly oriented pyrolitic graphite. *Physical Review Letters* 87(20):206401.

19. Esquinazi P, *et al.* (2009) Magnetic order in Graphite: Experimental evidence, intrinsic and extrinsic difficulties. *Journal of Magnetism and Magnetic Materials*.

20. Hahne R & Esquinazi P (2002) Can carbon be ferromagnetic? *Adv. Mater.* 14:753-756.

21. Barzola-Quiquia J, Esquinazi P, Rothermel M, Spemann D, & Butz T (2009) Magnetic order in proton irradiated graphite: Curie temperatures and magnetoresistance effect. *Journal of Nuclear Materials* 389(2):336-340.

22. Höhne R, *et al.* (2008) The influence of iron, fluorine and boron implantation on the magnetic properties of graphite. *Journal of Magnetism and Magnetic Materials* 320(6):966-977.

23. Turek P, *et al.* (1991) Ferromagnetic coupling in a new phase of the p-nitrophenyl nitronyl nitroxide radical. *Chemical Physics Letters* 180(4):327-331.

24. Han K, *et al.* (2003) Ferromagnetic spots in graphite produced by proton irradiation. *Advanced Materials* 15(20):1719-1722.

25. MURATA, *et al.* (1991) *Magnetic properties of amorphous-like carbons prepared from tetraaza compounds by the chemical vapour deposition (CVD) method* (Royal Society of Chemistry, Cambridge, ROYAUME-UNI) (0022-4936).

26. Ovchinnikov AA & Shamovsky IL (1991) The structure of the ferromagnetic phase of carbon. *Journal of Molecular Structure: THEOCHEM* 251:133-140.

27. Talapatra S, *et al.* (2005) Irradiation-Induced Magnetism in Carbon Nanostructures. *Physical Review Letters* 95(9):097201.

28. Pardo H, Faccio R, Araújo-Moreira FM, de Lima OF, & Mombrú AW (2006) Synthesis and characterization of stable room temperature bulk ferromagnetic graphite. *Carbon* 44(3):565-569.

29. Fujita M, Wakabayashi K, Nakada K, & Kusakabe K (1996) Peculiar localized state at zigzag graphite edge. *J. Phys. Soc. Jpn* 65:1920-1923.

30. Kobayashi Y (2006) Edge state on hydrogen-terminated graphite edges investigated by scanning tunneling microscopy. *Phys. Rev. B* 73:125415.

31. Niimi Y (2006) Scanning tunneling microscopy and spectroscopy of the electronic local density of states of graphite surfaces near monoatomic step edges. *Phys. Rev. B* 73:085421.

32. Son YW, Cohen ML, & Louie SG (2006) Half-metallic graphene nanoribbons. *Nature* 444:347-349.

33. Yazyev O & Helm L (2007) Magnetism induced by single-atom defects in nanographites. (Institute of Physics Publishing), pp 1294-1298.

34. Cervenka J & Flipse CFJ (2007) The role of defects on the electronic structure of a graphite surface. *J. Phys. Conf. Ser.* 61:190-194.

35. Cervenka J & Flipse CFJ (2009) Structural and electronic properties of grain boundaries in graphite: Planes of periodically distributed point defects. *Phys. Rev. B* 79:195429.

36. Parr R (1983) Density functional theory. *Annual Review of Physical Chemistry* 34(1):631-656.

37. Porezag D, Frauenheim T, Köhler T, Seifert G, & Kaschner R (1995) Construction of tight-binding-like potentials on the basis of density-functional theory: Application to carbon. *Physical Review B* 51(19):12947-12957.

38. El-Barbary AA, Telling RH, Ewels CP, Heggie MI, & Briddon PR (2003) Structure and energetics of the vacancy in graphite. *Physical Review B* 68(14):144107.

39. Yuchen M & et al. (2004) Magnetic properties of vacancies in graphene and single-walled carbon nanotubes. *New Journal of Physics* 6(1):68.

40. Telling RH, Ewels CP, El-Barbary AA, & Heggie MI (2003) Wigner defects bridge the graphite gap. *Nat Mater* 2(5):333-337.

41. Ovchinnikov AA & Spector VN (1988) Organic ferromagnets. *Synth. Mater.* 27:B615-B624.

42. Ferro Y, Marinelli F, & Allouche A (2003) Density functional theory investigation of the diffusion and recombination of H on a graphite surface. *Chemical Physics Letters* 368(5-6):609-615.

43. Sha X & Jackson B (2002) First-principles study of the structural and energetic properties of H atoms on a graphite (0 0 0 1) surface. *Surface Science* 496(3):318-330.

44. Duplock EJ, Scheffler M, & Lindan PJD (2004) Hallmark of Perfect Graphene. *Physical Review Letters* 92(22):225502.

45. Ruffieux P, Gröning O, Schwaller P, Schlapbach L, & Gröning P (2000) Hydrogen Atoms Cause Long-Range Electronic Effects on Graphite. *Physical Review Letters* 84(21):4910.

46. Brock A (2007) Medical Imaging: Equipment and Related Products. (BCC Research, Wellesley).

47. Bloch F, Hansen W, & Packard M (1946) Nuclear induction. *Physical review* 70(7-8):460-474.

48. Purcell E, Torrey H, & Pound R (1946) Resonance absorption by nuclear magnetic moments in a solid. *Physical review* 69(1-2):37-38.

49. Mansfield P & Morris P (1982) *NMR imaging in biomedicine* (Academic Press New York).

50. Lauterbur P (1973) Image formation by induced local interactions: examples employing nuclear magnetic resonance. *Nature* 242(5394):190-191.

51. Ernst R, Bodenhausen G, & Wokaun A (1990) *Principles of nuclear magnetic resonance in one and two dimensions* (Oxford University Press, USA).

52. Mackiewich B (1995) Basic Principles of MRI. (Simon Fraser University, Vancouver).

53. Brown M, Semelka R, & Nishino T (2004) MRI: basic principles and applications. *Medical Physics* 31:170.

54. Karen R. Sevigny Brown LGY (1997) Moyamoya Disease. in *Radiology Cases in Pediatric Emergency Medicine* (University of Hawaii John A. Burns School of Medicine ).

55. Rofsky N, *et al.* (1997) Peripheral vascular disease evaluated with reduced-dose gadolinium-enhanced MR angiography. *Radiology* 205(1):163.

56. Ruehm SG, Schmitz-Cristina H, Violas X, Corot C, & Debatin JF (2002) MR Angiography with a New Rapid Clearance Blood Pool Agent (P792): Initial Experience in Rabbits. *Academic Radiology* 9(2, Supplement 1):S407-S408.

57. Weissleder R, *et al.* (1990) Ultrasmall superparamagnetic iron oxide: characterization of a new class of contrast agents for MR imaging. *Radiology* 175(2):489.

58. Koh D, *et al.* (2004) Rectal Cancer: Mesorectal Lymph Nodes at MR Imaging with USPIO versus Histopathologic Findings—Initial Observations1. *Radiology* 231(1):91.

59. Ahlström K, *et al.* (1999) Pulmonary MR Angiography with Ultrasmall Superparamagnetic Iron Oxide Particles as a Blood Pool Agent and a Navigator Echo for Respiratory Gating: Pilot Study1. *Radiology* 211(3):865.

60. Schmiedl U, *et al.* (1987) Albumin labeled with Gd-DTPA as an intravascular, blood pool-enhancing agent for MR imaging: biodistribution and imaging studies. *Radiology* 162(1):205.

61. Flacke S, *et al.* (2003) Characterization of Viable and Nonviable Myocardium at MR Imaging: Comparison of Gadolinium-based Extracellular and Blood Pool Contrast Materials versus Manganese-based Contrast Materials in a Rat Myocardial Infarction Model1. *Radiology* 226(3):731.

62. Rohrer M, Bauer H, Mintorovitch J, Requardt M, & Weinmann H (2005) Comparison of magnetic properties of MRI contrast media solutions at different magnetic field strengths. *Investigative radiology* 40(11):715-724.

63. Wiener E, *et al.* (2005) Dendrimer-based metal chelates: a new class of magnetic resonance imaging contrast agents. *Magnetic Resonance in Medicine* 31(1):1-8.

64. Kumar K (1997) Macrocyclic polyamino carboxylate complexes of Gd (III) as magnetic resonance imaging contrast agents. *Journal of Alloys and Compounds* 249(1-2):163-172.

65. Port M, *et al.* (1999) P760 and P775: MRI contrast agents characterized by new pharmacokinetic properties. *Magnetic Resonance Materials in Physics, Biology and Medicine* 8(3):172-176.

66. Runge V, Kirsch J, & Lee C (2005) Contrast-enhanced MR angiography. *Journal of Magnetic Resonance Imaging* 3(1):233-239.

67. Anzai Y, *et al.* (2005) MR angiography with an ultrasmall superparamagnetic iron oxide blood pool agent. *Journal of Magnetic Resonance Imaging* 7(1):209-214.

68. Björk N, Ekstrand K, & Ruyter I (1986) Implant-fixed, dental bridges from carbon/graphite fibre reinforced poly (methyl methacrylate). *Biomaterials* 7(1):73-75.

69. Bokros J (1977) Carbon biomedical devices. *Carbon* 15(6):353-371.

70. Gott VL, Whiffen JD, & Dutton RC (1963) Heparin Bonding on Colloidal Graphite Surfaces. *Science* 142(3597):1297-1298.

71. Tetik RD, Galante JO, & Rostoker W (1974) A wear resistant material for total joint replacement - tissue biocompatibility of an ultra-high molecular weight (UHMW) polyethylene - graphite composite. *Journal of Biomedical Materials Research* 8(5):231-250.

72. Eriksson C & Nygren H (1997) The initial reactions of graphite and gold with blood. *Journal of Biomedical Materials Research* 37(1):130-136.

73. Olivares R, Rodil SE, & Arzate H (2007) Osteoinduction properties of graphite-like amorphous carbon films evaluated in-vitro. *Diamond and Related Materials* 16(10):1858-1867.

74. Starý V, Bacáková L, Horník J, & Chmelík V (2003) Bio-compatibility of the surface layer of pyrolytic graphite. *Thin Solid Films* 433(1-2):191-198.

75. Feng L, Hu CZ, & Andrade JD (1988) Scanning tunneling microscopic images of adsorbed serum albumin on highly oriented pyrolytic graphite. *Journal of Colloid and Interface Science* 126(2):650-653.

76. Orasanu A & Bradley R (2003) AFM and XPS study on albumin adsorption onto graphite surfaces. *Eur Cell Mater* 6(Suppl 2):46.

77. Bremerich J, Bilecen D, & Reimer P (2007) MR angiography with blood pool contrast agents. *European Radiology* 17(12):3017-3024.

78. Zheng J, *et al.* (2005) Single-session magnetic resonance coronary angiography and myocardial perfusion imaging using the new blood pool compound B-22956 (gadocoletic acid): initial experience in a porcine model of coronary artery disease. *Investigative radiology* 40(9):604.

79. Tuinstra F & Koenig J (1970) Raman spectrum of graphite. *The Journal of Chemical Physics* 53:1126.

80. Makarova T (2007) Magnetic properties of nanocarbon. *Diamond and Related Materials* 16(10):1841-1846.

81. Stöhr J (1992) *NEXAFS spectroscopy* (Springer).

82. Stoehr J (1992) Springer Series in Surface Sciences, vol. 25. *NEXAFS Spectroscopy*.

83. Brühwiler P, *et al.* (1995) ^{*} and ^{*} Excitons in C 1s Absorption of Graphite. *Physical Review Letters* 74(4):614-617.

84. Clarke J (1996) SQUID fundamentals. *SQUID Sensors: Fundamentals, Fabrication and Applications* 329:1–62.

85. Butz T, *et al.* (2005) The role of nuclear nanoprobes in inducing magnetic ordering in graphite. *Hyperfine Interactions* 160(1):27-37.

86. Esquinazi P & Hohne R (2005) Magnetism in carbon structures. *J. Magn. Magn. Mater.* 290-291:20-27.

87. Akgun H, Gonlusen G, Cartwright Jr J, Suki W, & Truong L (2006) Are gadolinium-based contrast media nephrotoxic?: A renal biopsy study. *Journal Information* 130(9).

88. Ye E, Liu B, & Fan WY (2007) Preparation of Graphite-Coated Iron Nanoparticles Using Pulsed Laser Decomposition of Fe3(CO)12 and PPh3 in Hexane. *Chemistry of Materials* 19(15):3845-3849.

89. Papadopoulos NG, *et al.* (1994) An improved fluorescence assay for the determination of lymphocyte-mediated cytotoxicity using flow cytometry. *Journal of Immunological Methods* 177(1-2):101-111.

90. Jacobsen MD, Weil M, & Raff MC (1996) Role of Ced-3/ICE-family proteases in staurosporine-induced programmed cell death. *The Journal of Cell Biology* 133(5):1041-1051.

91. Aderem A & Underhill D (1999) Mechanisms of phagocytosis in macrophages. *Annual review of immunology* 17(1):593-623.

92. Jutras I & Desjardins M (2005) Phagocytosis: at the crossroads of innate and adaptive immunity.